

# JGR Solid Earth

## RESEARCH ARTICLE

10.1029/2021JB022097

### Key Points:

- Complex attenuation structure in the Rocky Mountain region defies broad regionalization
- Sharp, high-scattering boundaries between adjacent provinces; these may require path-specific ground-motion predictions
- Evidence for *in situ* crustal melt in the southern Rockies and focused alteration and/or scattering in central and eastern United States sutures and tectonic zones

### Supporting Information:

Supporting Information may be found in the online version of this article.

### Correspondence to:

W. Levandowski,  
will.levandowski@tetrattech.com

### Citation:

Levandowski, W., Boyd, O. S., AbdelHameid, D., & McNamara, D. E. (2021). Crustal seismic attenuation of the central United States and Intermountain West. *Journal of Geophysical Research: Solid Earth*, 126, e2021JB022097. <https://doi.org/10.1029/2021JB022097>

Received 25 MAR 2021

Accepted 14 NOV 2021

### Author Contributions:

**Conceptualization:** Will Levandowski, Oliver Salz Boyd, Danya AbdelHameid, Daniel Edward McNamara

**Data curation:** Oliver Salz Boyd, Daniel Edward McNamara

**Formal analysis:** Will Levandowski

**Funding acquisition:** Will Levandowski

**Investigation:** Will Levandowski

**Methodology:** Will Levandowski, Oliver Salz Boyd, Daniel Edward McNamara

**Software:** Will Levandowski, Oliver Salz Boyd, Daniel Edward McNamara

**Validation:** Will Levandowski

**Visualization:** Will Levandowski, Danya AbdelHameid

**Writing – original draft:** Will

Levandowski, Danya AbdelHameid

**Writing – review & editing:** Will Levandowski, Oliver Salz Boyd, Daniel Edward McNamara

© 2021. American Geophysical Union.  
All Rights Reserved.

## Crustal Seismic Attenuation of the Central United States and Intermountain West

Will Levandowski<sup>1,2</sup> , Oliver Salz Boyd<sup>3</sup> , Danya AbdelHameid<sup>4</sup>, and Daniel Edward McNamara<sup>3,5</sup>

<sup>1</sup>Boulder Geophysics, Boulder, CO, USA, <sup>2</sup>Now at Tetra Tech, Inc., Boulder, CO, USA, <sup>3</sup>USGS Geologic Hazards Science Center, Denver, CO, USA, <sup>4</sup>The College of William and Mary, Alexandria, VA, USA, <sup>5</sup>Now at Daniel McNamara Consulting, LLC, Morgan Hill, CA, USA

**Abstract** Seismic attenuation is generally greater in the western United States (WUS) than the central and eastern United States (CEUS), but the nature of this transition or location of this boundary is poorly constrained. We conduct crustal seismic (Lg) attenuation tomography across a region that stretches from the CEUS across the Rocky Mountains to the Basin and Range using a total of 115,870 amplitude measurements from 106 earthquakes recorded on 544 stations across five frequency bands spanning 0.5–16 Hz. Similar to previous studies, we find higher attenuation in the WUS ( $Q_0 \sim 190$ ) than the nominally CEUS ( $Q_0 \sim 250$ ) and comparatively high attenuation on the Gulf Coast ( $Q_0 \sim 175$ ). Our models defy simple east versus west regionalization, however. Heterogeneity within the Rocky Mountain region—low attenuation in the Colorado Plateau interior and Wyoming Craton ( $Q_0 \sim 230$ ) compared to high attenuation in the southern Rockies ( $Q_0 \sim 110$ )—exceeds the gross differences between the CEUS and western United States. These province-scale patterns are readily interpreted in terms of intrinsic attenuation. The boundary between the Colorado Plateau and Basin and Range hosts the highest attenuation imaged in the study area ( $Q_0 \sim 90$ ), consistent with localized scattering across contrasting crustal structure. Focused high attenuation in the southern Rockies may represent the effects of represent *in situ* partial crustal melt. Within the CEUS, second-order bands of comparatively high attenuation align with the Proterozoic Yavapai-Mazatzal suture zone and Midcontinent Rift. This complex attenuation structure defies broad regionalization and suggests a need for path-specific models near these boundaries and for critical infrastructure.

**Plain Language Summary** Shaking dies away, or attenuates, with distance from an earthquake. Attenuation is slower in the eastern United States than the West, which greatly increases the area over which shaking is felt and damage can occur. Low seismicity rates in central North America have made it challenging to determine and understand the boundary between East and West, however. Recent manmade earthquakes in parts of Oklahoma and Colorado provide new data to map attenuation across the nation, and we find that there is not simple dichotomy between East and West after all. Instead, ancient tectonic events and modern processes combine to create a complex tapestry of attenuation. Understanding this complexity, however, will make it easier to forecast and prepare for seismic hazard.

## 1. Introduction

In areas with sparse seismicity such as the central and eastern United States (CEUS), the peak ground motions expected over time periods of years to decades are typically dominated by regional-distance (>100 km) surface waves (Petersen et al., 2014). Nevertheless, there are large differences in the decay of seismic energy with distance from the hypocenter—termed seismic attenuation—across the continental United States (e.g., Erickson et al., 2004; Gallegos et al., 2014, 2017; McNamara et al., 2014; Pasyanos, 2013).

The present study maps attenuation using amplitude decay of the crustal Lg phase, which is the dominant signal at regional distances (>~100 km) and frequencies of 0.5 Hz and higher. Lg has been observed to hypocentral distances of thousands of kilometer in stable continental regions (e.g., North Africa: McNamara & Walter, 2001). Therefore, a given earthquake may be recorded at hundreds of seismic stations, and a given seismic station may record Lg from many earthquakes. This redundancy allows robust separation of the impacts of source (i.e., earthquake) excitation, receiver-specific amplification, and path effects on the amplitude of the recorded shaking, each at a range of frequencies.

Previous Lg attenuation studies (e.g., Benz et al., 1997; Nuttli, 1973; Singh & Herrmann, 1983) have established the broad differences in attenuation between the western United States and CEUS. Other studies have isolated individual provinces inverted for single  $Q$  values for raypaths contained within those provinces (Erickson et al., 2004). Single-event linear transects have demonstrated a sharp boundary between the nominally cratonic portion of the CEUS and the Gulf Coast (Cramer, 2017). Pasyanos (2013) mapped crustal and upper mantle P-wave and S-wave  $Q$  structure across the conterminous United States (multiple frequencies were also used to constrain source and receiver terms and were inverted, but only 2–4 Hz tomograms were presented), similarly finding lower  $Q$  in the western United States (WUS) and Gulf Coast than in the CEUS for all phases. Attenuation tomography at  $\sim 1$  Hz (Gallegos et al., 2014) also depicts a disparity between the Gulf Coast and CEUS, as well as a correlation among attenuation values in the CEUS, heat flow, and sediment thickness. High-resolution  $Q$  models of the northeastern United States and southeastern Canada from 0.1 to 20.0 Hz (Zhao and Mousavi, 2018) display similar relationships and further feature more variability  $Q$  in the comparatively high-attenuation margins of the cratonic Canadian Shield than in its rather uniform low-attenuation interior. In summary, attenuation is generally higher in the West than the East, but substantial variability exists both within each region (e.g., Gulf Coast vs. CEUS interior; Colorado Plateau vs. Southern Rockies) and between individual models for a given location. Consequently, regionalization of ground-motion prediction equations applicable to crustal surface waves and delineation of province boundaries has been challenging in the Intermountain West (IMW), Rocky Mountains, and Great Plains.

Within the past decade, however, the Transportable Array has traversed the CEUS and hundreds of moderate-magnitude induced earthquakes have occurred in Oklahoma and southern Kansas, central Arkansas, northern and eastern Texas, the Denver Basin, and the Raton Basin (Colorado/New Mexico). This increase in human-induced seismicity exposes more Americans to substantial annualized seismic hazard (Petersen et al., 2016) and does so in regions with the substantial uncertainty in attenuation structure mentioned above. Nevertheless, these same earthquakes have improved source coverage by as much as a factor 100 or more in some areas, availing new constraints on 2D crustal attenuation structure, seismic source excitation, and site amplifications.

At present, the USGS National Seismic Hazard Model (NSHM) divides CEUS and WUS along a boundary estimated from physiography and several geophysical markers, chiefly seismicity rate (Frankel et al., 1996). Different ground motion models are applied east and west of this boundary, so its location may impact seismic hazard assessments for nearly 20 million people and building codes for potentially billions of dollars of construction. Despite this societal importance, this article is the first of which we are aware specifically designed to image the CEUS/WUS attenuation boundary. Using refined amplitude kernels that account for the effects of off-raypath forward scattering and data from 106 earthquakes at frequencies from 0.5 to 16 Hz, we produce a new tomographic model of about half of the continental United States, centered on the Rocky Mountains–Great Plains transition (Figure 1), that can inform probabilistic estimates of shaking in both 1-yr and long-term NSHMs and more precisely delineate the CEUS/WUS attenuation boundary than previously possible.

## 2. Approach

### 2.1. Data Set

We choose waveforms of moderate-magnitude ( $M_w = \sim 3.2$  to 5.3) earthquakes from a region from Oklahoma in the east to the eastern Basin and Range in the west, straddling the Rocky Mountains (Figure 1 and Table S2). Path lengths are limited to 110–1,600 km to avoid contamination of Lg by other phases. Earthquake depths less than 20 km ensure that the Lg waves were generated in and remained in the crust. Waveforms were inspected for the appearance of Lg on the vertical component.

Amplitudes as functions of frequency are defined by spectral power of vertical displacement throughout a time window corresponding to the range of propagation velocities from 3.0 to 3.6 km/s. For example, at 360 km hypocentral distance the time window ranges from 100 to 120 s after the origin. Instrument response functions are deconvolved from the windowed velocity seismograms to yield absolute ground displacement in meters. The displacement time series are Fourier transformed into the frequency domain, and the power spectrum is measured as the root-mean-squared (RMS) power over non-overlapping whole octaves for five bands with center frequencies at 0.75, 1.5, 3.0, 6.0, and 12.0 Hz (frequencies 0.5–1, 1–2, 2–4, 4–8, and 8–16 Hz, respectively). For example, measuring RMS amplitude over 2.0–4.0 Hz for the center frequency of 3.0 Hz reduces the variance relative to



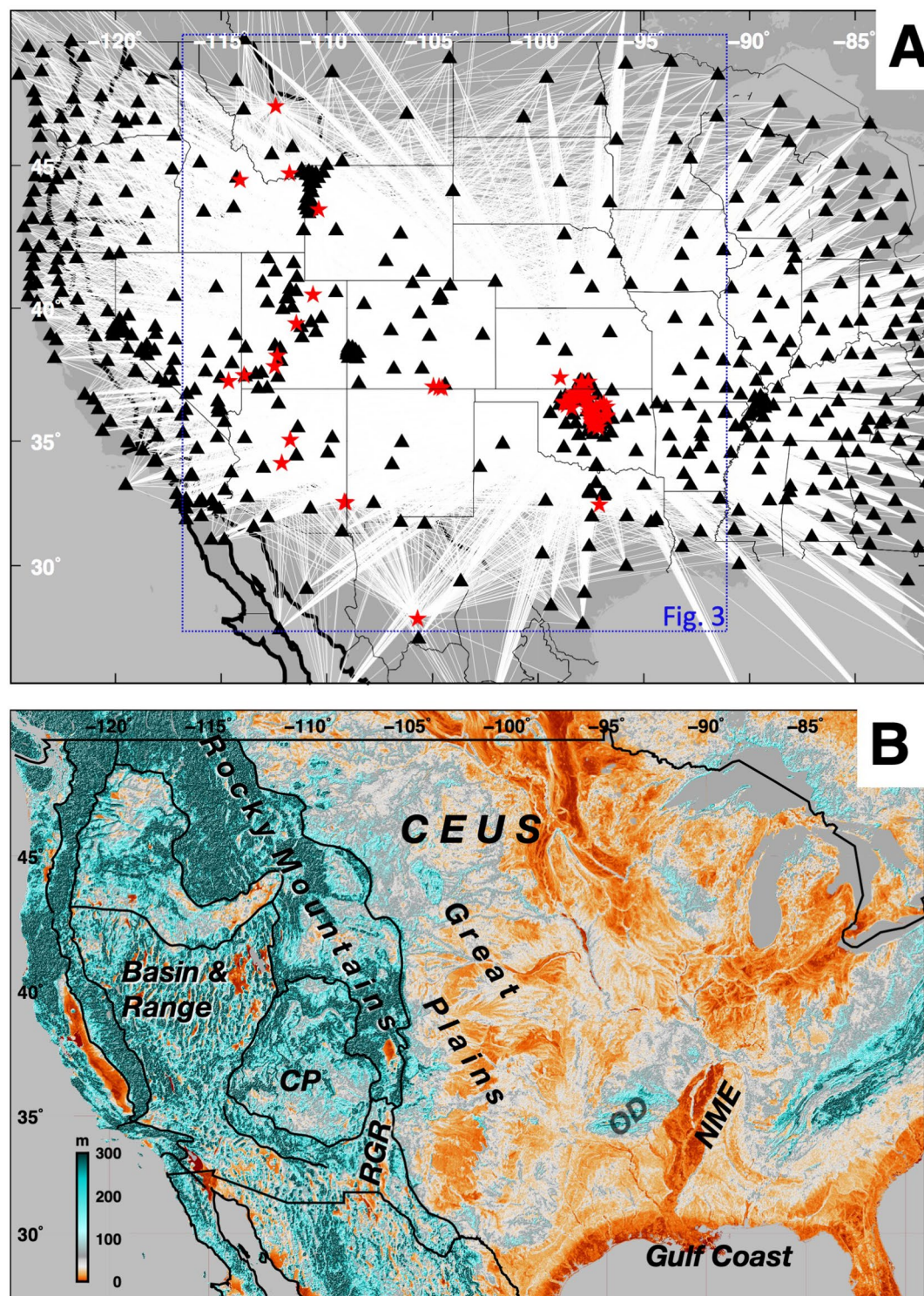


**Figure 1.** Data. (a) Lg raypaths (white). Red stars: Earthquakes ( $n = 106$ ). Black triangles: Stations ( $n = 544$ ). The main study area is shown by the blue box. (b) Major physiographic provinces (black outlines). Background shading: Maximum prominence over 3 km radius (highest elevation minus lowest) (Brandenburg et al., 2017) using 30 arc-second topography. Abbreviations. CP, Colorado Plateau; NME, Northern Mississippi Embayment; OD, Ozark Dome; RGR, Rio Grande Rift.

measuring peak amplitudes, which are relatively more sensitive to outliers. Data with signal/noise (defined as RMS Lg amplitude/RMS P-coda amplitude)  $<2$  were rejected. Finally, in order to ensure overdetermined source and receiver terms, each event must be recorded by at least four receivers and each receiver must record at least four events.

The quality-controlled dataset comprises 106 earthquakes recorded at 544 stations (Figure 1a), with 115,870 individual amplitude observations (Figure 2a). Earthquakes are recorded by an average of 219 stations at each frequency, and stations record an average of 42 earthquakes at each frequency. Amplitude—and therefore signal/noise—decreases with frequency (Figure 2), so the number of accepted recordings generally decreases with increasing frequency: 38,661 at 0.75 Hz, 34,462 at 1.5 Hz, 20,846 at 3 Hz, 7,646 at 6 Hz, and 12,455 at 12 Hz. Consequently, tomographic resolution degrades with increasing frequency.

## 2.2. Methods

In order to explicitly decompose the recorded amplitude of Lg at frequency  $f$  into source, receiver, and attenuation factors, it is common (e.g., Benz et al., 1997; Erickson et al., 2004; McNamara et al., 2014; Pasyanos, 2013) to consider the amplitude as the product of energy loss due to geometrical spreading, a source excitation term, a receiver-specific amplification term, and exponential energy loss with distance:

$$A_{ij}(f) = D_{ij}^{-\gamma} S_j(f) R_i(f) e^{-\pi f D_{ij} / Qv} \quad (1)$$

$D_{ij}$  is the hypocentral distance from source  $j$  to receiver  $i$ .  $S$  is the earthquake- and frequency-specific source amplitude.  $R$  is the receiver-specific site-amplification factor. The geometrical spreading factor,  $\gamma$ , is assumed to be 0.5 (following McNamara et al., 2014 and many others), and  $v$  is the average crustal shear velocity ( $\sim 3.5$  km/s for Lg). Finally,  $Q$  is the “quality factor,” the inverse of attenuation. Any tradeoff between  $v$  and  $Q$  will have minor effect on resolved  $Q$  because vertically averaged shear velocity in North American continental crust may range from  $\sim 3$  to  $\sim 3.6$  km/s ( $\pm 10\%$ ; McNamara et al., 1996), whereas  $Q$  varies by a factor of 2 or more at a given frequency.

$$\ln(A_{ij}) + \gamma \ln(D_{ij}) = \ln(S_j) + \ln(R_i) - \left( \frac{\pi f D_{ij}}{v} \right) 1/Q \quad (2)$$

In Equation 2, the left-hand side subsumes the factors that are known or assumed, and the right-hand side comprises the three terms of interest that must be inverted for: source excitation  $S$ , receiver-specific site amplification  $R$ , and attenuation  $1/Q$ . Choosing an arbitrary reference value  $\ln(R_{\text{ref}}) = 0$ ,  $R_i$  represents a scalar multiplier by which amplitudes at a given site are amplified or dampened—for  $\ln(R) > 0$  and  $\ln(R) < 0$ , respectively—relative to the reference. The median  $R$  at a given frequency can therefore be chosen as the reference for simplicity.

At all frequencies considered, there is a first-order linear relationship between the left-hand side and distance (Figure 2a). The slope of this line is proportional to attenuation, or  $1/Q$ , and the best-fit  $Q$  at each frequency is listed in Figure 2.  $Q$  increases with frequency, approximately with  $f^{0.9}$ . Closer consideration reveals that the y-intercept of this line is most readily interpreted as the average source excitation at a given frequency: If the median receiver—with  $\ln(R)$  equal to 0—were located at the hypocenter, the geometrical spreading, attenuation, and receiver terms would vanish, leaving  $\ln(A) = \ln(S)$ . Deviations from the linear fit therefore represent the combined effects of variations in path-averaged attenuation,  $R$ , and variations in  $S$  (e.g., as a function of magnitude).

In practice, the quantity to which amplitudes are sensitive is apparent  $Q$  because both intrinsic (e.g., thermally dependent) attenuation and scattering attenuation, as well as any lateral variations in geometrical spreading (Morozov, 2008), will contribute to energy loss. Although efforts are made below to qualitatively separate intrinsic and scattering attenuation, the possible effects of variable geometric spreading are not considered. As general rules, these effects will be subsumed by the total apparent attenuation and interpreted as intrinsic rather than scattering, and the practical impact of combining variable geometrical spreading and apparent attenuation on seismic hazard estimates will be minimal.



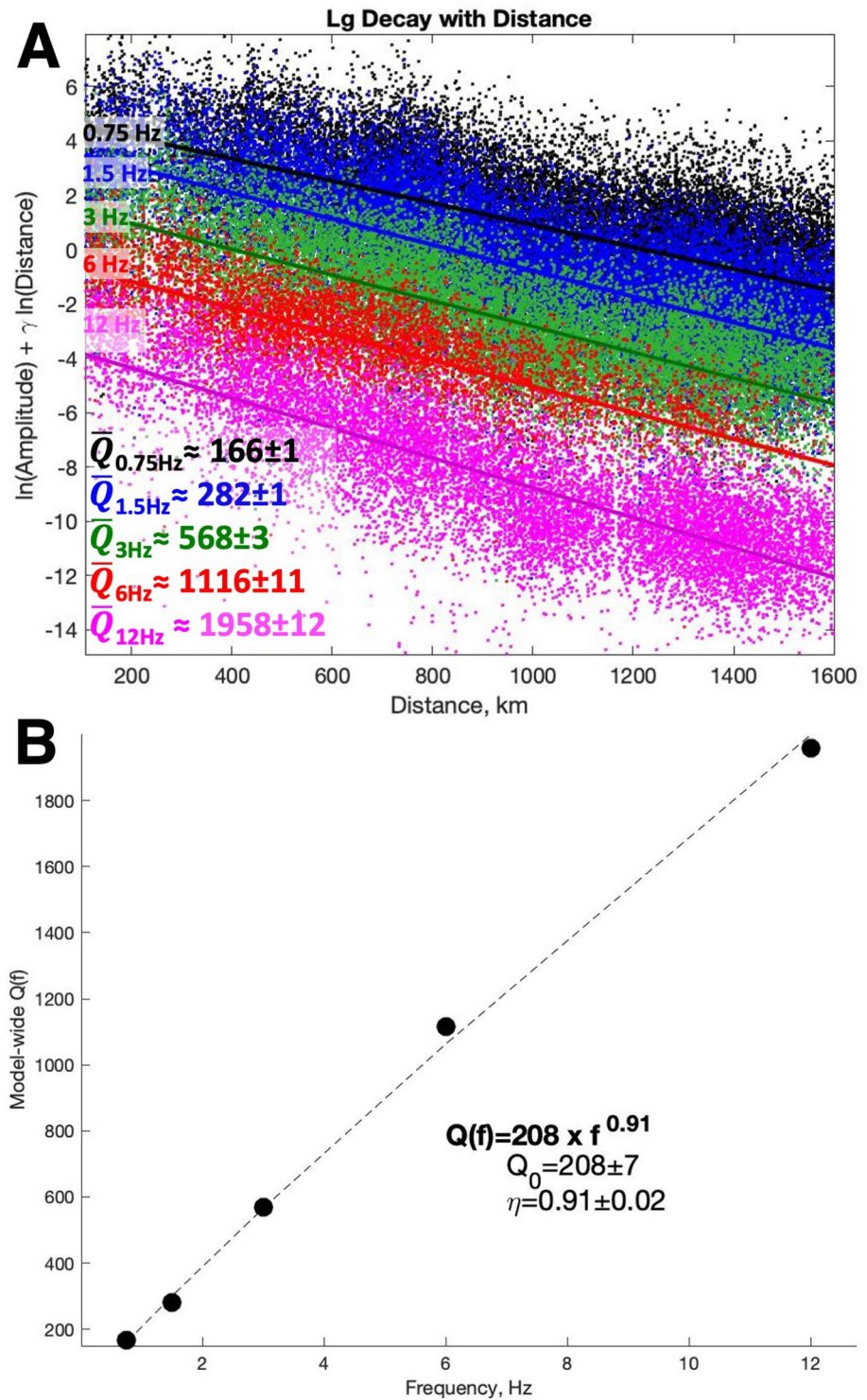


**Figure 2.** Data. (a) Amplitudes adjusted for geometrical spreading versus hypocentral distance. Dots: Adjusted amplitude, colored according to frequency. The best semi-log linear fit at each frequency is shown as bold colored lines; slopes are proportional to  $1/Q(f)$ . Associated  $Q$  values are listed with  $1\sigma$  uncertainties. (b) Frequency dependence of the model-wide  $Q(f)$  fits shown in Figure 1a.  $Q$  increases with frequency, roughly as  $f^{0.91}$ .

### 2.3. Tomography

Framed as a tomographic problem, a study region is readily discretized into  $k$  elements (e.g., cells or nodes), such that the shaking at receiver  $i$  due to earthquake  $j$  is given by  $S_j$ ,  $R_i$ , and the integrated—here, discretized and summed—impacts of attenuation in each element:

$$\ln(A_{ij}) + \gamma \ln(D_{ij}) = \ln(S_j) + \ln(R_i) - \left( \frac{\pi f}{v} \right) \sum_k D_{ijk} / Q_k \quad (3)$$

In Equation 3,  $D_{ijk}$  is the distance that energy traveling from source  $j$  to receiver  $i$  travels through element  $k$ . Commonly (e.g., Benz et al., 1997; Erickson et al., 2004; McNamara et al., 2014), inversions are conducted independently for each frequency (band). Subsequently, these single-frequency results can be qualitatively synthesized or combined in a more quantitative fashion. We perform independent joint inversions for  $S_j(f)$ ,  $R_i(f)$ , and  $Q_k(f)$  for each of the five frequency bands.

A novel component of this work is the computation of finite-width sensitivity kernels for ground motion amplitudes. The RMS amplitude over a time window does not depend exclusively on the  $Q$  structure along the direct raypath. Instead, the sensitivity kernels for Lg amplitude are analogous to the Fresnel zone. Taking the example of 360 km hypocentral distance once again, a time window ranging from 100 to 120 s is used to compute the frequency-amplitude spectrum. All forward-scattered Lg energy that arrives within 20 s of the energy along the direct great-circle path will impact the ground motions at the receiver over some portion of the time window used to calculate spectral amplitudes. A path that has an adjoint travel time of 110 s will contribute energy to half of the time window used. Because a point along this path will influence half of the time series that will be Fourier transformed, its relative weight will be half that of points along the direct ray. Thus, the spatial sensitivity kernel has finite width, such that off-path heterogeneity influences amplitudes. The relative amplitude of the kernel depends inversely on the adjoint (source-to-anomaly-to-receiver) travel time. Sensitivity peaks along the minimum travel time path and decays to 0 for adjoint travel times equal to hypocentral distance divided by 3 km/s. The resulting amplitude is a function of the integrated weighted attenuation structure of all points along such paths. Synthetic feature recovery tests using these novel kernels and more traditional formulations are presented in Figures S1–S3 in Supporting Information S1.

Finally, the study area is parameterized by  $k$  nodes with 2D-continuous  $1/Q$  structure between them, rather than discrete cells of internally uniform  $1/Q$ . The effective value of  $1/Q$  at any point in the model is the inverse-distance-weighted average of the surrounding four nodes. The practical impact of this parameterization is that the final term in Equation 3 becomes an integral rather than summation. That term would be a path integral for infinitely thin sensitivity kernels only along the great-circle source-to-receiver path but takes the form of a surface integral when the finite-width sensitivity kernels are employed.

Lateral variations in  $1/Q$  are subjected to a frequency-dependent smoothing matrix (penalty function). The weights of this penalty for differences in  $1/Q$  between cell  $k$  and  $k'$  are proportional to  $f$  and inversely related to  $D_{kk'}$ . Increased smoothing coefficients with frequency are a necessary corollary to decreasing  $1/Q$  with frequency. A leading coefficient was chosen by  $L$ -curve Tikhonov analysis of model norm versus data residual norm of all frequencies. A value of  $\sim 40f$  was found to fall near the inflection point for all five frequencies and so was chosen for internal consistency.

The inversions use a two-stage singular value decomposition and node spacing of  $\sim 50$  km. The data vector is the amplitude residuals relative to a uniform  $Q$  and  $S$  model. This data vector is depicted graphically as the scatter about the linear fit at a given frequency in Figure 2. The resulting model vector represents perturbations to  $1/Q$ , variations in  $S$ , and the  $R$  terms.

### 2.4. Frequency Dependence

After performing the inversions independently for each frequency band, it is informative to synthesize information across the frequency spectrum. The frequency dependence of  $Q$  is often modeled as:

$$Q(f) = Q_0 f^n \rightarrow \ln(Q(f)) = \ln(Q_0) + n \ln(f) \quad (4)$$

Although there is no specific physical reason that this relationship should exist (e.g., Pasyanos, 2013), it is a useful heuristic to combine models at different frequencies and to investigate spatial variations in the frequency dependence of  $Q$ . Reference relations were derived from model-wide (i.e., uniform- $Q$ ) least-squares fits in Figure 2b:

$$\ln(Q(f)) \approx \ln(208) + 0.91 \ln(f) \rightarrow Q(f) \approx 208 f^{0.91},$$

$$Q_0 = 208 \pm 7; n = 0.91 \pm 0.02$$

Scattering attenuation can depend more strongly on frequency than intrinsic attenuation, with scattering typified by  $n$  of 1.0 or greater and intrinsic attenuation by  $n$  of 0.7 or less (e.g., Mayeda et al., 1992). Additionally, the total attenuation is the linear sum of intrinsic and scattering attenuation:

$$1/Q_{\text{total}} = 1/Q_{\text{intrinsic}} + 1/Q_{\text{scattering}} \quad (5)$$

Therefore, if two regions have similar intrinsic attenuation, the region with greater scattering will display lower  $Q$  overall and higher frequency dependence  $n$ .

After solving the inverse problem independently for each of the five frequency bands, an equation of the form of Equation 4 is fit to the empirical  $Q$  values to determine  $Q_0$  and  $\eta$ .

### 3. Results

Amplitude data from each of the five frequency bands are inverted independently for their respective  $1/Q$ ,  $S$ , and  $R$ . Since the frequency bands do not overlap, these models are nominally as independent as if they were derived for different earthquakes recorded at different stations. Although resolution degrades with increasing frequency because the number of accepted Lg waveforms decreases (hence the increasing uncertainties listed in Figure 2a), all five  $Q$  models display similar patterns. Therefore, discussion focuses on  $Q_0$  (Figure 3a), which leverages up to five unique constraints, each derived from overdetermined inversions of the form of similar form to Equation 3. Results for the individual frequency bands are presented in Figures 3b–3f. Resolution and recovery tests on single-frequency tomography are presented in Figure 4; frequency dependence and source and receiver terms are summarized in Figure 5.

Our  $Q$  tomograms are consistent with previous work but offer finer resolution in the region bounded by the events used in the inversion. The IMW ( $Q_0 \sim 150$ ) broadly has lower  $Q$  than the CEUS ( $Q_0 \sim 250$ ), but these regions are not uniform. Within the IMW, the Colorado Plateau ( $Q_0 \sim 250$ ) displays  $Q$  at least as high as the average CEUS, and the Gulf Coast ( $Q_0 \sim 175$ ) stands out from the surrounding CEUS with grossly similar attenuation to the IMW.

#### 3.1. Intermountain West

The generally attenuative IMW is interrupted by the high- $Q$  Colorado Plateau ( $Q_0 \sim 250$ ), which is separated from the Southern Rockies to the east and Basin and Range to the west by abrupt transitions ( $\lesssim 200$  km). In fact, a continental minimum in  $Q$  ( $Q_0 \sim 100$ ) appears in a narrow approximately N–S zone along the western margin of the Colorado Plateau. This exceptionally high-attenuation band is not coincident with the western edge of Colorado Plateau as a physiographic province but extends about 100 km inboard. Similarly, the attenuation boundary between the Southern Rockies and Colorado Plateau encroaches  $\sim 100$  km westward into the physiographic Plateau. This pattern is consistent with the conceptual model of Roy et al. (2009): Partially intact continental lithospheric mantle beneath the Plateau (e.g., Lee et al., 2001) may be undergoing progressive thermochemical alteration, from the periphery toward the Plateau interior, by fertile asthenosphere, and/or subduction-related fluids (Levandowski, Jones, Butcher, & Mahan, 2018).

The Colorado Plateau does not appear to be entirely isolated from other stable portions of the continental United States, however. The partially intact interior of the Colorado Plateau appears also in (high) upper mantle velocities (e.g., Shen & Ritzwoller, 2016), in (low) heat flow (e.g., Blackwell et al., 2011), in (low) earthquake rates (e.g., Mueller, 2019), and in the deviatoric crustal stress field (NNE–SSW tension) (Levandowski, Herrmann, Briggs, Boyd, & Gold, 2018), suggesting links among thermochemical structure of the lithosphere and crustal



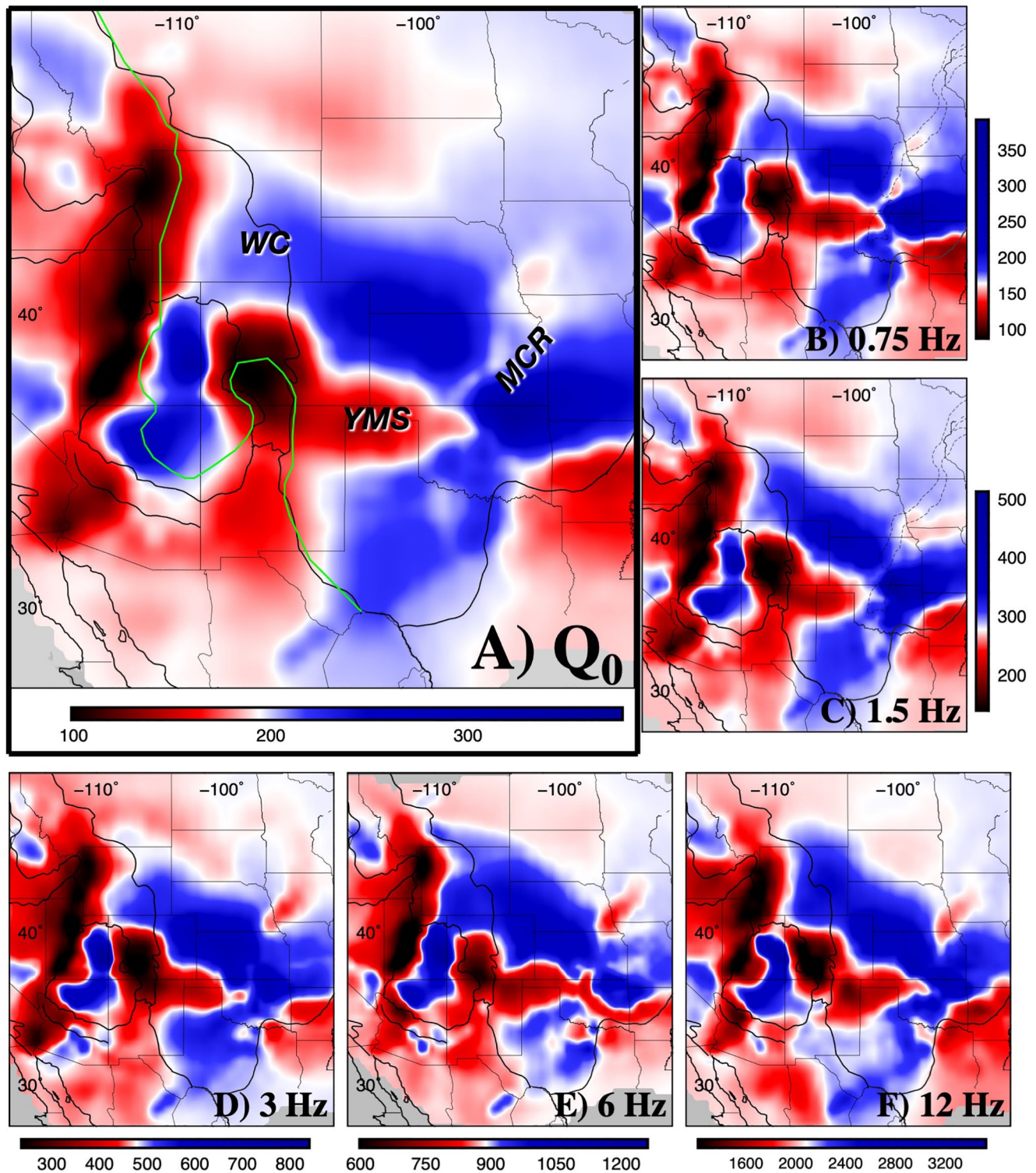


**Figure 3.**  $Q$  tomograms. Individual frequencies are shown in (b–f). Results are synthesized as  $Q_0$  in (a) to facilitate comparison across frequencies, colorscale intervals are fixed to the same quantiles for each frequency (e.g., median value is always white). Areas discussed in the text noted in (a). *Abbreviations.* MCR, Midcontinent Rift; SRM, Southern Rocky Mountains; WC, Wyoming Craton; YMS, Yavapai-Mazatzal Suture Zone.



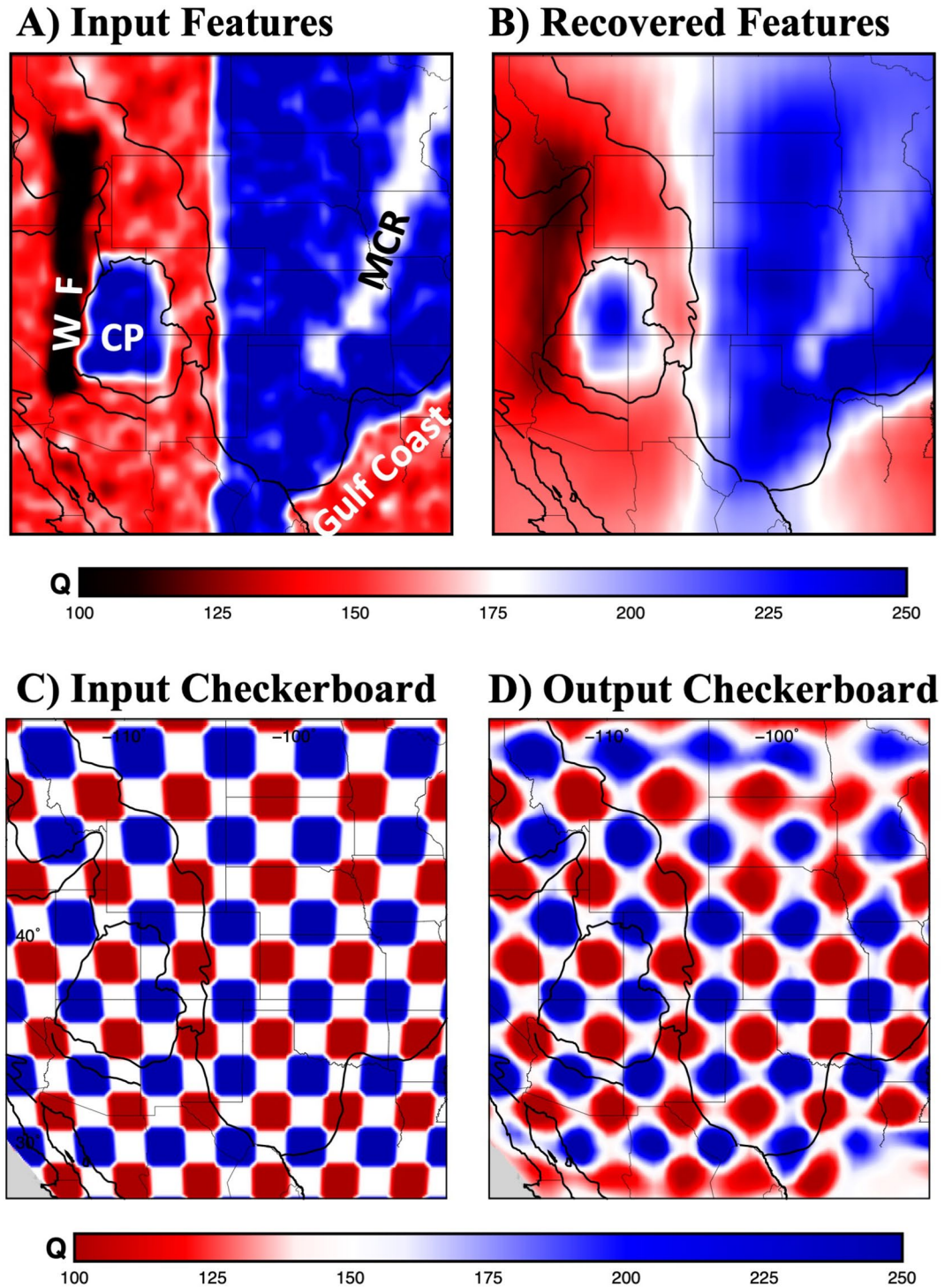
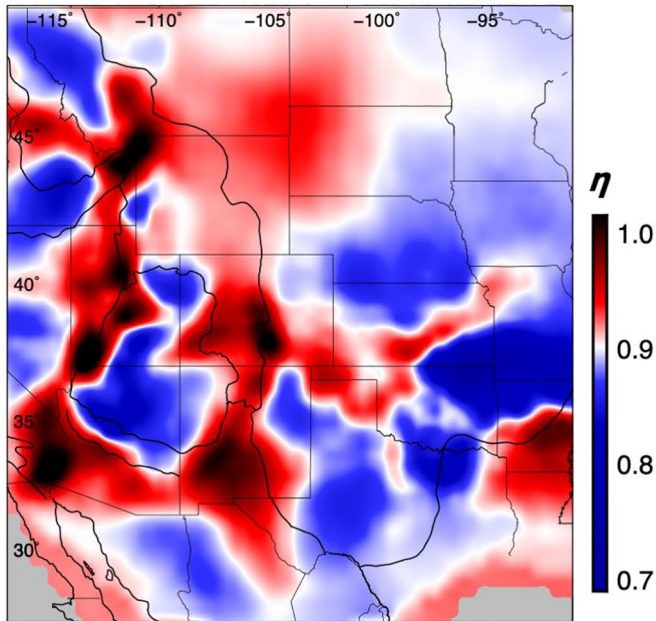
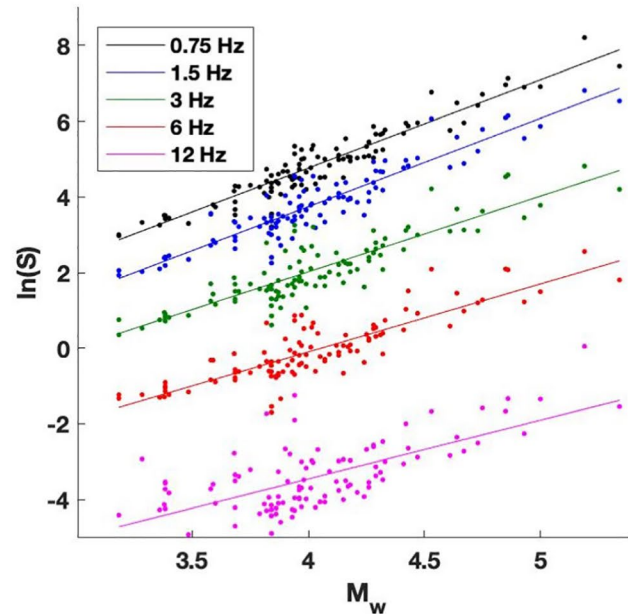


**Figure 4.** Model tests. (a) Feature recovery input mimics the Colorado Plateau/Basin and Range boundary (i.e., Wasatch Front, WF;  $Q = 100$ ), Colorado Plateau ( $Q = 250$ ), and Midcontinent Rift (MCR;  $Q = 180$ ). Uniform  $Q = 150$  is applied on the Gulf Coast and west of  $-105^\circ$ ;  $Q = 250$  elsewhere. (b) Output model images long, skinny tectonic features (100 s of km  $\times$  100–200 km MCR and WF) and isolated anomalies (275 km  $\times$  500 km Colorado Plateau) and correctly locates the change in attenuation. (c) Checkerboard test with alternating 200-km rows/columns of high/low (250–100) anomalies on  $Q = 150$  background. All features discussed in the text are substantially larger than 200 km  $\times$  200 km. (d) Output checkerboard recovers every input block in this region. More resolution tests are presented in Supporting Information S1.

**A) Frequency dependence,  $\eta$**



**B) Source terms vs. magnitude**



**C) Receiver terms**

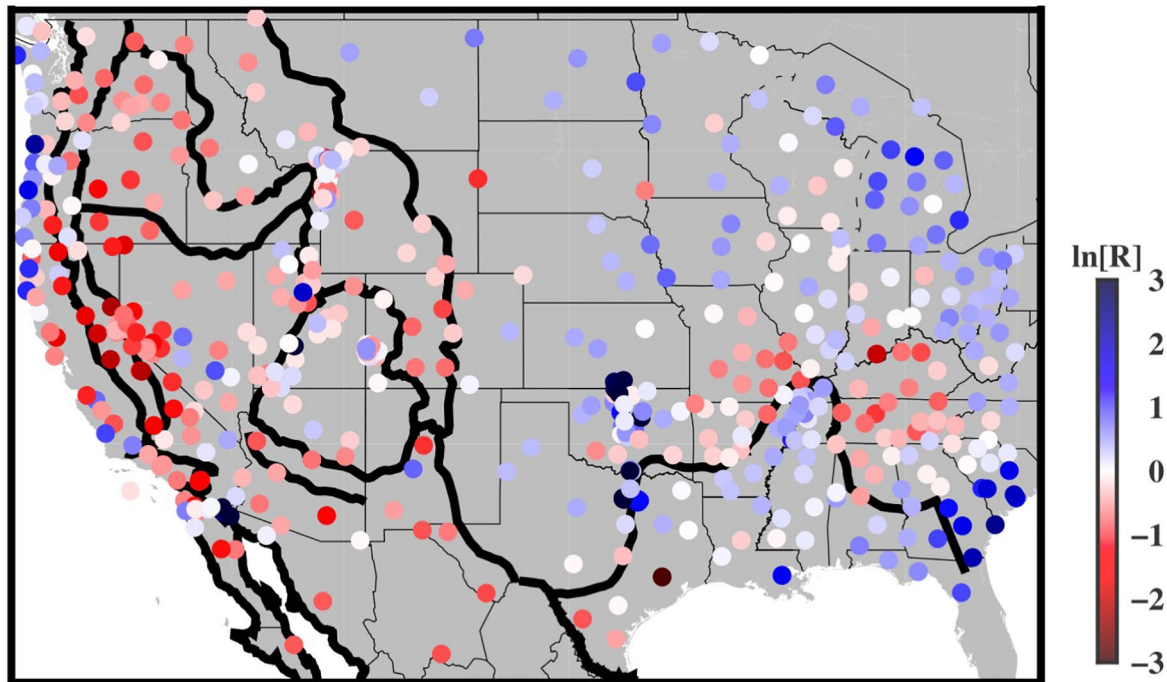


**Figure 5.** Other model elements. (a)  $\eta$ : An equation of the form  $Q(f) = Q_0 f^\eta$  is fit at each node. Anomalously high  $\eta$  mainly aligns with tectonic and physiographic boundaries, especially the Colorado Plateau/Basin and Range and the Great Plains/Rockies boundaries, as well as the Gulf Coast and Midcontinent Rift. (b) Source terms: The linear relationship between empirical  $\ln(S)$  and  $M_w$  substantiates the linear relationship between  $S$  and moment:  $\ln(S)$  is roughly proportional to  $2M_w$  (e.g.,  $\ln(S_{0.75\text{Hz}}) \sim \alpha \sim 2.2 M_w$ ;  $\ln(S_{12\text{Hz}}) \sim \alpha \sim 1.6 M_w$ ). Additional variations may result from near-source velocity and density variations and variations in stress drop, among other factors. (c) Receiver terms are presented in full in Figure S7 in Supporting Information S1 and Table S2. Each station's average  $R$  across the five frequencies is presented here. Site response accounts for  $\pm 3$  ln-unit amplification/damping (400-fold variation in ground motion). CEUS sites generally have higher  $R$  than the WUS, and the Mississippi Embayment, Gulf Coast, and Atlantic Plain host the greatest amplification.

deformation. The same stress field, high velocities, low heat flow, and sparse seismicity, as well as high  $Q$ , continue northward into the crust above the partially intact lithospheric keel of the Wyoming Craton ( $Q_0 \sim 230$ ). Furthermore, this Colorado Plateau/Wyoming Craton meta-province is not bounded within the Cenozoic-active IMW region but rather is continuous with the low heat flow, high velocities, WNW-ESE extension, low background seismicity rates, and high  $Q$  of the northern Great Plains ( $Q_0 \sim 250$ – $350$ ), well into the CEUS. Thus, these  $Q$  patterns are more closely correlated with lithospheric structure rather than physiography or presence/absence of Cenozoic deformation.

High attenuation in the Basin and Range is well documented (e.g., Pyle et al., 2017). We image modestly higher  $Q$  in the central Basin and Range ( $Q_0 \sim 210$ ) and the lowest  $Q$  along the boundary between the Colorado Plateau and the Basin and Range ( $Q_0 \sim 100$ ). Overall, however, the Basin and Range merges imperceptibly with the rest of the IMW—aside from the Colorado Plateau/Wyoming Craton—to form a broad province of internally consistently low  $Q$  ( $Q_0 \sim 100$ – $200$ ), low seismic velocities, high heat flow, and approximately E-W extension. With important implications for regionalization, the southern Rockies fall within this zone, whereas  $Q$  increases abruptly across the eastern range front of the southern Rockies onto the Great Plains. Unlike the Colorado Plateau/Rockies boundary to the west, the Plains/Rockies attenuation boundary is nearly coincident with the physiographic boundary along strike, although the magnitude of this change varies from  $\sim 25\%$  between the Rio Grande Rift ( $Q_0 \sim 170$ ) and southern Plains ( $Q_0 \sim 215$ ) to more than 100% from the southern Rockies ( $Q_0 \sim 110$ ) to central Plains ( $Q_0 \sim 300$ ).

### 3.2. CEUS

As observed in cratonic portions of southeastern Canada (e.g., Zhao and Mousavi, 2018),  $Q$  remains broadly uniformly high (here,  $Q_0 > 220$ ) across nominally stable parts of the CEUS, with notable high-attenuation zones around the margins. These mobile belts are typically sites of ancestral deformation and have mostly been active during multiple episodes of differing deformation styles.

Chief among these border regions is the Gulf Coast ( $Q_0 \sim 175$ ), where high attenuation is well documented. As noted by Cramer (2018), the division between the high- $Q$  CEUS and lower  $Q$  Gulf Coast may step northward along inherited rift structures. Because tomography effectively averages over azimuths and distance ranges, it cannot resolve the locations and frequency dependence of small features or sharp gradients with the precision of the single-event transects of Cramer (2018).

A second high-attenuation feature bounding the cratonic CEUS roughly coincides with the Proterozoic Yavapai-Mazatzal suture zone (Whitmeyer & Karlstrom, 2007), which has been a locus of cryptic, recurring tectonism. Ancestral Rockies contraction reanimated the suture zone as the Las Animas Arch, and faults also accommodated secondary, highly oblique deformation during the Laramide (Zellman et al., 2021). Subsequently, the suture zone experienced anomalous post-mid-Miocene flexural uplift (Leonard, 2002), and it hosts modestly elevated rates of modern seismicity (e.g., Mueller, 2019), including the Holocene-active Cheraw Fault along its northern flank (e.g., Crone et al., 1997). The suture zone is characterized by a notable isostatic residual gravity low (e.g., Abrams & Knepper, 1994), and although it hosts lower- $V$ s middle and lower crust than its surroundings (e.g., Shen & Ritzwoller, 2016), the gravity anomaly is more pronounced than expected from typical velocity-density relationships (Levandowski et al., 2017). Xenoliths document hydrous mantle near the Cheraw Fault (Davis & Smith, 1993). Hydrous crustal material could explain the anomalous velocity-density relationship, leading to the suggestion that fluids exsolved from the Farallon slab may have been channeled along the inherited lithospheric-scale fractures within this suture zone, focusing hydration-induced retrogression (Levandowski et al., 2017). In this case, the localized high attenuation may be intrinsic. Alternatively or in combination, the lithospheric-scale discontinuity and other, later faults in this area may scatter incoming energy.

The Midcontinent Rift (MCR) has similarly been active at multiple times since the Proterozoic and also is marked by modestly elevated attenuation ( $Q_0 \sim 210$ ). The MCR experienced extension and two phases of mafic volcanism at 1,109–1,106 and 1,100–1,094 Ma (Davis & Green, 1997; Miller et al., 2002), with sedimentation both during rifting and subsequently as a result of thermal subsidence. Whether rifting was the result of a mantle plume (e.g., Vervoort et al., 2007 and references therein) or far-field stress associated with the rifting of Amazonia from Laurentia (Stein et al., 2014), within 20 Myr of the cessation of MCR extension, crustal normal faults inverted and accommodated substantial shortening and crustal thickening, likely due to far-field compression associated



with the Grenville Orogeny (Gordon & Hempton, 1986; McWilliams & Dunlop, 1978). There is evidence of some additional shortening across the southern portion of the MCR during the latest Mississippian(?), perhaps due to far-field stresses from the Appalachian events (Pangaea assembly), and more substantial reactivation occurred during the Pennsylvanian-Permian Ouachita and Ancestral Rockies Orogenies; a final, minor period of faulting approximately coincided with the latest Cretaceous Laramide Orogeny (Burberry et al., 2015). The multiply activated faults, localized sedimentation, volcanics and intrusions, and possible thermochemical alteration could all play a role in creating the observed high attenuation.

### 3.3. Uncertainty, Resolution, and Recovery Tests

Three types of resolution tests have been conducted. First, feature recovery tests validate the inversion algorithm's ability to image structures similar to those expected in the study area including dichotomous CEUS/WUS structure, very high attenuation along the Colorado Plateau/Basin and Range boundary, high attenuation on the Gulf Coast, moderate attenuation along the MCR, and the low attenuation Colorado Plateau (Figures 4a and 4b; Figures S1–S3 in Supporting Information S1). Checkerboard tests are also presented (Figures 4c and 4d; Figure S4 in Supporting Information S1); these demonstrate that features as small as 50 km × 50 km could be imaged in Oklahoma and along the Basin and Range/Colorado Plateau border, but some small features (~150 km × 150 km) in the northeastern part of the study area (i.e., the northcentral United States) may be missed. In both cases, a synthetic  $Q$  structure is generated, the amplitudes are forward modeled along the raypaths used in this study, and these synthetic data (with or without noise added) are then inverted to examine how well the known  $Q$  structure can be recovered. Finally, the uncertainty in model values with respect to the dataset is assessed by jackknife resampling the events used in the inversion and examining the variance in output models (Figures S5 and S6 in Supporting Information S1). These tests are discussed more fully in Supporting Information S1.

### 3.4. Source Terms

The amplitude of shaking intuitively depends on the magnitude of the earthquake. (Moment tensors are available USGS, 2016 for ~80% of the events. For other events, we use the conversions detailed by Mueller, 2019 to estimate  $M_w$ .) At all frequencies, there is a linear relationship between  $\ln S$  and  $M_w$  (Figure 5a). Specifically,  $\ln(S)$  is approximately proportional to  $2M_w$  at intermediate frequencies, such that a  $M_w 5$  event produces four  $\ln$ -units (54 times) the shaking of a collocated  $M_w 3$  event recorded at the same station. A  $M_w 6$  would produce about 400 times the motion as a  $M_w 3$ , if this trend continues beyond the magnitude range of events used here.

Source information is compiled in Table S1, which lists date, time, hypocentral location, magnitude, and the  $\ln(S)$  at each of the five frequencies.

The exponential empirical relationship between  $S$  and moment is consistent with the formulation of Walter and Taylor (2001):

$$S(f) = \phi M_0 / \left( \frac{f_c + f}{f_c} \right)^2 \quad (6)$$

The term  $\phi$  encapsulates the effects of near-source density and velocity (Pasyanos et al., 2009):

$$\phi \approx \frac{0.05}{\sqrt{\rho_{source} v_{source}^5}} \quad (7)$$

### 3.5. The Corner Frequency $f_c$ is Directly Related to Stress Drop $\Delta\sigma$

$$f_c = K v_{source} (\Delta\sigma / M_0)^{1/3} \quad (8)$$

The term  $K$  depends on rupture velocity, radiation pattern, elastic constants, and rupture model (Brune, 1970, 1971; Madariaga, 1976; Sato & Hirasawa, 1973; Savage, 1972) yet ranges only from ~0.28 to 0.49.

Therefore, there is a robust linear relationship between  $S$  and moment, or  $\ln(S)$  and  $M_w$ , and departures from this regression are most easily explained by stress drop and near-source structure. Such phenomena empirically account for approximately  $\pm 1$  ln-unit (i.e., between 3 times and 1/3 as much) variations in ground motion.

Furthermore, analysis of magnitude-to-source term scaling is the topic of ongoing research beyond the scope of this article.

### 3.6. Receiver Terms (Site Response)

Conditions local to each seismic station influence the amplitude of ground motion. The reference value of  $R$  is arbitrary, so we choose the median value at each frequency. (The average  $R$  is indeed very near to 0 in each inversion.) Therefore, the values of  $R$  represent the factors by which local conditions amplify or dampen motion for an arbitrary earthquake at an arbitrary distance. Many of the seismic stations used in this work lie outside the footprint of the earthquakes used, and we note above that the results of our  $Q$  tomography should be considered preliminary outside of this footprint, yet we suggest that the  $R$  determined are likely robust because they are overdetermined to a great degree, with stations recording an average of 219 events overall and 44 at any given frequency. Moreover,  $R$  for any given site is generally consistent across frequencies (Figure S7 in Supporting Information S1). Because the inversion at each frequency is independent of the others, this consistency lends substantial additional credence to the robustness of these site amplification factors. For simplicity, this brief discussion focuses on each station's average  $\ln(R)$  value across the five frequencies (Figure 5c). Station information and  $\ln(R)$  models for each frequency are compiled in Table S2.

Consistent with previous work, site response is greater in the CEUS than the IMW, and this pattern is observed at all frequencies. Spatial patterns are typified by lengthscales of 10–100 s of km, reflecting the geologic control on site response. In particular, areas with substantial sedimentary cover—including the Gulf Coast, Atlantic coastal plain, and Mississippi Embayment—experience higher ground motions than hard-rock sites. The latter is exemplified in the negative  $R$  observed in the Ozark Dome (Figure 5c; see Figure 1b for location).

As with source terms, detailed examination of Lg site response is warranted. Even when averaged across all frequencies to limit spurious results (Figure 5c), site-specific values of  $\ln(R)$  range from  $-3$  ln-units (1/20th the average shaking) to  $+3$  ln-units (20 times the average). Thus, site conditions alone can account for 400-fold variations in ground motion amplitudes. This 400-fold difference parallels the 400-fold difference between  $M_w 6$  and  $M_w 3$  extrapolated above: A very low- $R$  hard-rock site would experience similar ground motions at a given distance from a  $M_w 6$  to a high-amplification site the same distance from a  $M_w 3$ . Given the importance of these terms, their thorough investigation is beyond the scope of this article.

## 4. Discussion

### 4.1. Comparison With Prior Studies

Because Lg amplitudes can be measured to hypocentral distances well exceeding 1,000 km, numerous prior studies have examined Lg attenuation from the scale of individual provinces to much of continental North America. The precision and spatial resolution of these previous studies vary, as do the frequency ranges used and the methods employed. As an unsurprising result, the specific values of  $Q$  also vary widely between models at a given location. The values of  $\eta$  are even more widely scattered, so discussion focuses on  $Q_0$ .

### 4.2. Single-Event and Single-Station $Q$ Estimates

Studies prior to the modernization of seismic networks in the CEUS did not have sufficient resolution to delineate individual features but documented broad, regional variations. Coda  $Q$  estimates from Herrmann (1980) and Singh (1981) combined geometrical spreading and attenuation in one parameter, finding multiple CEUS values clustered near 1,000, compared to  $\sim 330$  for station DUG (Dugway, UT, USA) and 140 for BKS (Berkeley, CA, USA). Removing the effects of geometric spreading and using a semi-log linear fit, the CEUS values rescale to near  $Q \approx 600$ . Singh and Herrmann (1983) expanded their crustal coda dataset and retrieved similar patterns and values.

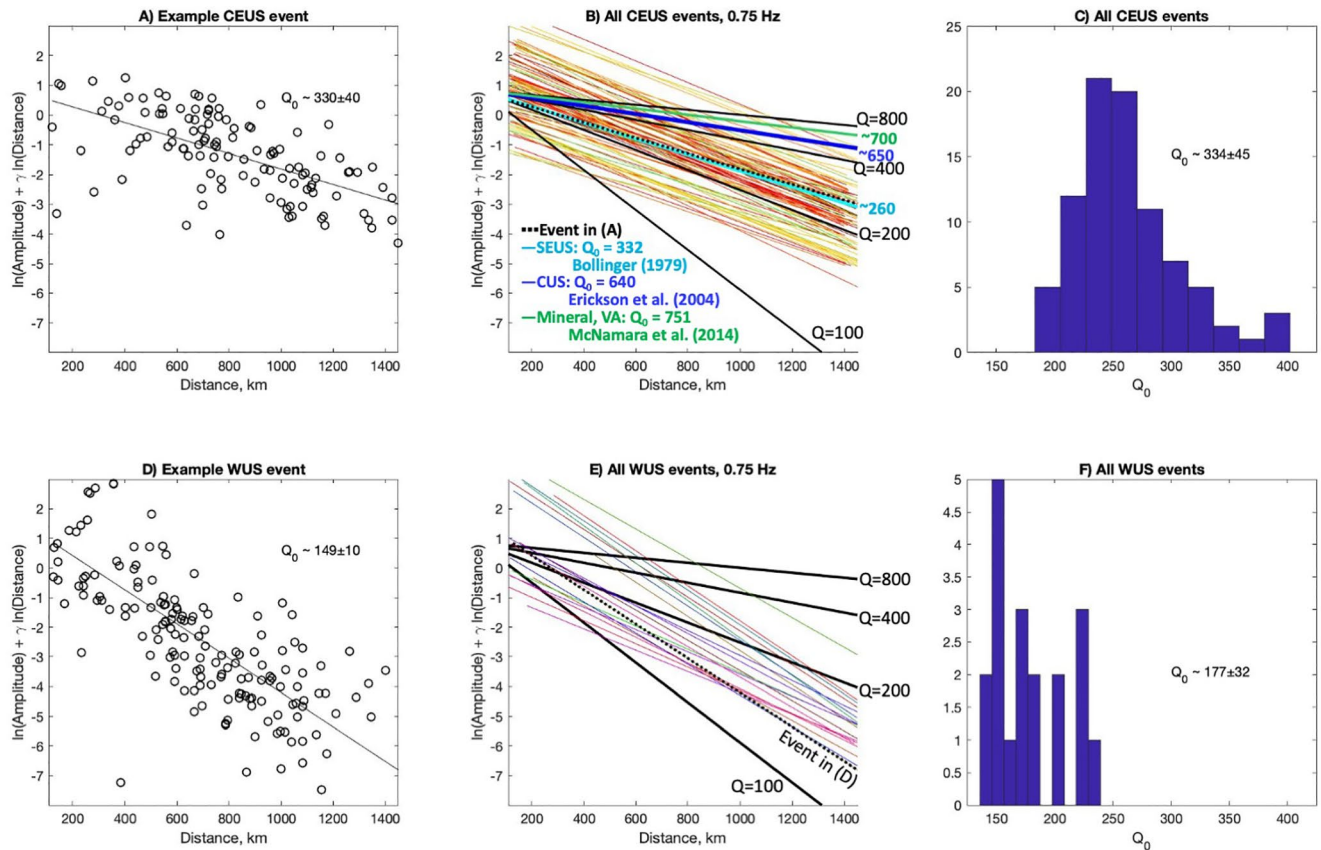


**Figure 6.** (a) log-Amplitude versus distance for a CEUS event recorded on CEUS stations (east of  $-104^\circ$ ) at 0.75 Hz (circles). The slope of the regression (black line) is proportional to  $Q_{0.75\text{Hz}}$ .  $Q_0$  is estimated for  $\eta = 0.85$ . (b) Regressions for each CEUS event. The dashed line matches the regression line in (a) Bold black lines: Reference lines for  $Q_{0.75\text{Hz}} = 100, 200, 400$ , and  $800$  with y-intercepts set to a typical value. Fits following the same procedure to CEUS data from other Lg studies (with y-intercepts set to that typical value). (c) Single-event  $Q$  estimates for all CEUS events on CEUS stations. (d) log-Amplitude versus distance for a WUS event recorded on WUS stations (west of  $-104^\circ$ ) at 0.75 Hz (circles). The slope of the regression (black line) is proportional to  $Q_{0.75\text{Hz}}$ .  $Q_0$  is estimated for  $\eta = 0.85$ . (e) Regressions for each WUS event. The dashed line matches the regression line in (d) Bold black lines: Reference lines for  $Q_{0.75\text{Hz}} = 100, 200, 400$ , and  $800$  with y-intercepts set to a typical value. (f) Single-event  $Q$  estimates for all WUS events on WUS stations.

Dwyer et al. (1983) revisited the problem using bandpass-filtered amplitude data to make frequency-dependent  $Q$  calculations from several CEUS events and found much lower  $Q_{1\text{Hz}}$  (cf.,  $Q_0$ ) of  $\sim 330$ . Early tomographic inversions (Baquer & Mitchell, 1998) revealed the same trends, but with average CEUS  $Q_0 \sim 550$ . This value accords with single-province frequency-dependent Lg  $Q$  values— $\sim 650$  in both the central and northeastern United States—and contrasts with  $\sim 200$  in the Basin and Range, and between 100 and 200 in the Rockies, California, and Cascadia (Erickson et al., 2004). Cramer (2018) delineated the Gulf Coast/CEUS boundary at discrete frequencies using single-event transects. Although designed to provide precise constraints on the boundary location, the amplitude-distance curves also estimate  $Q_0 \sim 259$  in the Gulf Coast and  $\sim 500$  in the CEUS.

To allow direct comparison with other Lg studies, we calculate single-event best-fit  $Q$  for CEUS events recorded on the CEUS stations (Figures 6a–6c) and for WUS events recorded in the WUS (Figures 6d–6f). The log-amplitudes corrected for geometric spreading (the left-hand side of Equation 3) are regressed onto distance, such that the slope is proportional to  $1/Q$ , and apparent  $Q$  for each event is determined. CEUS events display significantly higher apparent  $Q$  than WUS events, yet no individual event displays a best-fit constant  $Q$  much above 400. Spreading-corrected amplitude versus distance fits from Bollinger (1979) for New Madrid events ( $Q_0 \sim 330$ ), Erickson et al. (2004) for southeastern/southcentral United States events ( $Q_0 \sim 640$ ), and McNamara et al. (2014) for Mineral, VA aftershocks ( $Q_0 \sim 750$ ) are overlain on our CEUS fits (Figure 6b). At a given distance, amplitudes from the latter two areas, which are east of the primary focus of our model, are simply higher than ours, justifying the lower  $Q$  reported here. By contrast, Bollinger's (1979) data—reported for 1 Hz and rescaled to 0.75 Hz here—from near the eastern edge of study area accord with the range of  $Q$  values in our tomography.



We cannot say why others (also see below) find much higher  $Q_0$  values, in some cases greatly exceeding 1,000; the amplitude versus distance data in Figures 2 and 6 clearly demonstrate that such values are inconsistent with our octave-averaged displacements. Differences could arise from the use of displacement instead of velocity or spectral acceleration, the use of RMS power over whole octaves rather than peak power or power at a specific period, or—for other tomographic studies, discussed below—the inversion algorithm (LSQR, singular value decomposition, etc.) and smoothing/damping parameters, among others.

### 4.3. CEUS Tomography

Especially since the passage of the Earthscope Transportable Array, several tomographic inversions for 2D  $Q$  structure have been conducted in and including the continental United States. Broadly across North America, Lg  $Q_0$  peaks at nearly 1,000 in the Canadian Shield, has local maxima near 700 in the northeastern United States and the Ozark Dome (located in the central United States; see Figure 1), and low values along Gulf and Atlantic Coasts ( $Q_0 \sim 400$ ) and Pacific margin ( $Q_0 \sim 200$ ; Mitchell et al., 2015). Targeting the continental United States at higher resolution, Pasyanos(2013) developed a multi-phase  $Q$  model in which effectively non-attenuating patches of the CEUS ( $Q_{\text{sCrustal3Hz}} \gg 1,000$ ) several 100 km across alternate with larger regions of moderate  $Q$  ( $Q_{\text{sCrustal3Hz}} \sim 300\text{--}800$ ), suggesting issues with inversion regularization where  $1/Q$  approaches 0. Only the 3 Hz tomogram is presented—and only graphically—and frequency dependence is not quantified; here and in Table S3 we use  $\eta \sim 0.8$  to approximate  $Q_0 \approx Q_{\text{s3Hz}}/(3^{0.8}) \approx Q_{\text{s3Hz}}/2.4$ . Overall, crustal  $Q_s$  is lower in WUS ( $Q_{\text{sCrustal3Hz}} \sim 250\text{--}400$ ;  $Q_0 \sim 110\text{--}165$ ) than CEUS (average  $Q_{\text{sCrustal3Hz}} \sim 600$ ;  $Q_0 \sim 300$ ) and lowest of all on the Gulf Coast ( $Q_{\text{sCrustal3Hz}} \sim 175$ ;  $Q_0 \sim 75$ ).

Two-station and reverse two-station methods were employed for 1-Hz Lg  $Q$  tomography of the central United States, from the Rocky Mountain Front at  $-105^\circ$  longitude to  $-80^\circ$  longitude (Gallegos et al., 2014). These methods use common-source amplitude ratios ( $\sim 39,000$  and  $4,600$  ratios, respectively), to nullify source-side effects and source and site terms, respectively. Both models display high attenuation in extended regions of the southcentral United States—average  $Q_0 \sim 400$  through the Gulf Coast, Mississippi Embayment/Reelfoot Rift, and Southern Oklahoma Aulacogen—compared to the bulk of the CEUS ( $Q_0 \sim 700$ ). Both models also include an ENE-trending high- $Q$  zone, that is, bounded on its northwest side by the MCR. Two-station  $Q$  drops from  $\sim 1,600$  to  $\sim 450$  at the MCR over  $\sim 200$  km distance and remains near 600 northwest of the MCR, while the reverse two-station model decreases more gently from 1,600 to  $\sim 600$  at the MCR but immediately jumps back to 1,600 northwest of the MCR. We also find anomalous moderate  $Q$  along the western arm of the MCR ( $Q_0 \sim 210$ ) and generally lower  $Q$  in the Precambrian core of North America northwest of the MCR than in the Proterozoic terranes. Nevertheless, undulations of nearly 1,000  $Q$  units over as little as 100 km laterally are ubiquitous in both the Gallegos et al. (2014) two-station and reverse two-station models, and the locations and amplitudes of these spikes differ between the two models, hindering direct comparison with our results.

Unlike the models of Pasyanos(2013) and Gallegos et al. (2014), our model lacks patches of  $Q > 1,000$ . This difference likely arises from differences in the inversion algorithms. Our method uses a much slower yet more stable singular value decomposition than the LSQR algorithm employed by Gallegos et al. (2014). Using LSQR and/or reducing the smoothing coefficient determined from Tikhonov  $L$ -curve inflections can easily allow our inversions to return isolated  $Q$  values exceeding 1,000 at low frequencies. Inversions can even return physically impossible negative attenuation. Nevertheless, the reduction of data residual variance associated with relaxed regularization is small compared to the increase in model variance, not justifying the increased model complexity. The choice of inversion setup and smoothing coefficients are key, because smoothing operators fail to suppress lateral variations in  $Q$  as  $1/Q$  becomes small: small decreases in  $1/Q$  that do not appreciably reduce residual amplitude cause attendant  $Q$  values to balloon, yet the small change in  $1/Q$  is not heavily penalized by the smoothing operator. Thus, it is likely that the high  $Q$  values and extreme lateral variations in some prior  $Q$  tomograms result from a breakdown in the regularization of iterative inversions as  $Q$  values become small.

### 4.4. Western United States

Separately, Gallegos et al. (2017) constrained site response spectra with reverse two-station data and then inverted the more plentiful two-station paths with site-specific amplitude adjustments for Lg  $Q$  tomograms at 0.5, 1, 2, and 3 Hz central frequencies. The technique was applied only to the WUS because of technical challenges associated

with the order-of-magnitude dynamic range of  $Q$  values between WUS minima ( $\sim 100$ ) and CEUS maxima ( $\sim 1,000$ ). As a result, these models—and the earlier central U.S. models (Gallegos et al., 2014)—are of limited use in locating and characterizing the CEUS/WUS/Rockies boundary.

In the limited overlap between the Gallegos et al. (2017) WUS study and the footprint of events used in the present study, results are grossly similar (Figures S8–S10 in Supporting Information S1). Because Gallegos et al. (2017) do not fit  $Q_0 f^n$  to individual tomography cells, comparisons must be made at individual frequencies. Common features include a high- $Q$  Colorado Plateau (this study/Gallegos et al., 2017;  $Q_0 \sim 250$ –230) that connects with a similarly high- $Q$  Wyoming Craton and an isolated moderately high- $Q$  region in the southcentral Basin and Range ( $Q_0 \sim 350$ –380). The Rio Grande Rift also has high attenuation in both models ( $Q_0 \sim 130$ –150). Results are less consistent from frequency to frequency in the Gallegos et al. (2017) model than in ours, however. Gallegos et al. (2017) find low  $Q$  in the southern Rockies and Yellowstone at some frequencies but not at others. Similarly, the Colorado Plateau/Basin and Range boundary—the Wasatch Front—is marked by a zone of high attenuation at some frequencies while high attenuation bands cross-cut the boundary at other frequencies. By contrast, our models display a boundary-parallel exceptionally high-attenuation band at all frequencies and consistently high attenuation in the southern Rockies and Yellowstone. We find high  $Q$  within the Wyoming Craton and low  $Q$  along its eastern margin at all frequencies, yet the two-station models include substantial variations in the trend, amplitude, and polarity of anomalies at different frequencies. From W or SW to E or NE across the Craton, Gallegos et al. (2017) find NW-trending high/low/high  $Q$  undulations and a low- $Q$  eastern margin at 0.5 Hz, a lower-amplitude north-trending high/low pair and high- $Q$  margin at 1 Hz, north-trending high/low/high anomalies and a high- $Q$  margin at 2 Hz, and ENE-trending high/low/high/low/high bands with high  $Q$  along the eastern margin at 3 Hz.

#### 4.5. Frequency Dependence

The frequency dependence of attenuation,  $\eta$  (Figure 5a), is moderately correlated with  $Q_0$ , suggesting that there may be some tradeoff between the two. For example,  $\eta$  approaches 1.0 in many parts of the high-attenuation Colorado Plateau margins but remains below 0.8 within the stable Plateau interior. Some correlation between  $Q_0$  and  $\eta$  is expected (Equations 5 and 6), however: Empirically, the two quantities share a Pearson correlation coefficient of 0.58. Therefore, despite small nominal uncertainties in  $\eta$  (Figure S11 in Supporting Information S1) relative to the amplitude of spatial variations, we intentionally temper interpretations based primarily on  $\eta$ .

The highest- $n$  zones ( $\eta \gtrsim 0.95$ ) in our model are confined to tectonic boundaries and major tectonic elements. We find high  $n$  along the Colorado Plateau/Basin and Range boundary ( $\eta > 1.0$ ), but the interior of the central Basin and Range has comparatively low  $n$  ( $\sim 0.86$ ) that more closely resembles the CEUS ( $\eta \sim 0.85$ ). Parts of the northern Mississippi Embayment and much of the Gulf Coast margin similarly host high  $n$  ( $\sim 0.95$ ). The final notable anomaly in the region enclosed by the sources used in this study roughly coincides with the southernmost extent of the western arm of the MCR ( $\eta \sim 0.93$ ). The localized low- $Q$  anomalies in these areas are consistent with focused attenuation by scattering features, a supposition, that is, bolstered by the comparatively high  $\eta$  values and explored below.

#### 4.6. Scattering Zones

The boundaries discussed above are typically local maxima in attenuation and coincide with sites of major—often lithospheric-scale—tectonic events. As seen in Equations 5 and 6, even if these zones have identical intrinsic attenuation to one of the adjacent blocks, localized scattering could elevate total attenuation.

The specific structural control on this hypothesized scattering cannot be determined from our models, but crustal thickness changes are a possibility in several cases. Because Lg samples the entire crustal column, substantial energy is reflected or scattered by crustal thickness decreases. Conversely, crustal thickness jumps spread incoming energy over a greater depth range, essentially diluting the energy. Therefore, apparent  $Q$  will be anomalously low in regions with steep lateral crustal thickness gradients, regardless of whether waves travel from thin to thick crust or from thick to thin. Indeed, Moho depth decreases from 40 to 45 km in the Colorado Plateau to  $\sim 30$  km in the Basin and Range over a lateral distance of  $\sim 100$  km, and the Gulf Coast margin marks a drop of roughly 15 km (e.g., Shen & Ritzwoller, 2016).

Scattering could also give rise to locally high attenuation via mechanisms other than changes in crustal thickness. The eastern and southern edges of the Wyoming Craton, the Proterozoic Yavapai-Mazatzal suture zone, and the portion of the MCR resolved with this source-receiver distribution all display locally anomalous low  $Q$  without such large crustal thickness variations, if any, across them (e.g., Shen & Ritzwoller, 2016). We suspect that crustal-scale faults inherited from continental suturing or focused extension then inversion—which also have been reactivated multiple times since—may scatter incoming energy.

#### 4.7. Crustal Melt in the Southern Rockies

The southern Rockies do not have substantially different crustal thickness from the Colorado Plateau to the west or the Great Plains to the east, so high attenuation is not readily explained by crustal thickness changes. Moreover, while the Rockies/Plains boundary is nearly coincident with the range front, the  $Q$  boundary between the Rockies and the Plateau is generally some 100–200 km west of the physiographic boundary, within the Plateau. The sharp eastern boundary is similar to the longer-period (0.02–0.1 Hz) upper mantle attenuation tomograms of Boyd and Sheehan (2005), who made quantitative comparisons with shear-velocity models to argue that the low mantle  $Q$  beneath the eastern edge of the southern Rocky Mountains results from high mantle temperatures. By contrast, there is not agreement among crustal  $Q$ , mantle velocity, and mantle  $Q$  in southwestern Colorado. Both mantle velocity (e.g., Shen & Ritzwoller, 2016) and crustal  $Q$  are even lower than near the range front, but mantle  $Q$  is modestly higher in the Boyd and Sheehan (2005) study. Although its origin is ambiguous, the potential mismatch between upper mantle velocity and upper mantle  $Q$  in southwestern Colorado is plausibly due to hydration (e.g., replacement of olivine by phlogopite; Boyd & Sheehan, 2005).

Recent magnetotelluric tomography (Feucht et al., 2017) reveals compelling evidence for *in situ* melt beneath much of the southern Rockies. The eastern and western boundaries of this interpreted melt zone are nearly identical to our  $Q$  boundaries. To the west, both boundaries lie 100–200 km into the physiographic Colorado Plateau, but the eastern boundary of the southern Rockies' low  $Q$  and the eastern edge of interpreted melt both fall closely along the range front between the Rockies and Great Plains. Partial melt within the crust would indeed greatly increase attenuation (Hammond & Humphreys, 2000), yet magnetotelluric signals are chiefly sensitive to the conductivity-thickness product and so cannot uniquely resolve the thickness of the zone of possible melt. Feucht et al. (2017) note that their magnetotelluric results alone leave ambiguity among a ~10% partial melt zone throughout the lower 25 km of the crust; a ~1.5 km zone of either nearly 100% partial melt or saline fluid trapped beneath an impermeable boundary; or a hybrid scenario in which melt-filled, N-S, near-vertical dikes feed a set of narrow sills, and exsolved volatiles pond above these sills in the mid crust. Noting active E-W extension in the area (Berglund et al., 2012), weak volcanism, and electrical anisotropy with higher conductivity in a N-S direction, they ultimately favor the latter explanation.

Our attenuation model also supports the latter interpretation, of a system fed by deeper melts. Peak seismic reflection amplitude occurs where scatterer thickness is equal to one quarter-wavelength (~1 km for 0.75 Hz Lg; ~75 m for 12 Hz Lg). Therefore, we hypothesize that if melt pockets are indeed responsible for low  $Q$  because of both intrinsic and scattering effects, these pockets could have typical widths anywhere from tens to more than hundreds of meters thick. As a result, we also favor the scenario of near-vertical dikes feeding a volatile-rich zone in the mid crust. The fluids invoked by Feucht et al. (2017) could be cogenetic with the proposed (Boyd & Sheehan, 2005) hydrated upper mantle, at least in southwestern Colorado. Because N-S melt-rich lenses would more profoundly scatter energy propagating across the Rockies, further work examining attenuation anisotropy could provide additional constraints.

#### 4.8. Temperature, Velocity, and Intrinsic Attenuation

The zones discussed above—the Colorado Plateau and Wyoming Craton and their edges, the Yavapai-Mazatzal suture zone, and the MCR—subsume most of the short spatial-wavelength variation in our models: The continental United States is otherwise characterized as a set of broad  $Q$  provinces. This zonation roughly aligns with tectonic and/or physiographic provinces. We interpret these broad zones in terms of intrinsic attenuation.

Support for this hypothesis comes from the striking similarity among spatial patterns in long-wavelength crustal  $Q$ , heat flow (and temperatures inferred therefrom), and lithospheric seismic velocity. These correlations are demonstrated in Figures 7a and 7b. Specifically,  $1/Q_0$  is plotted against estimated temperature at 10 km depth



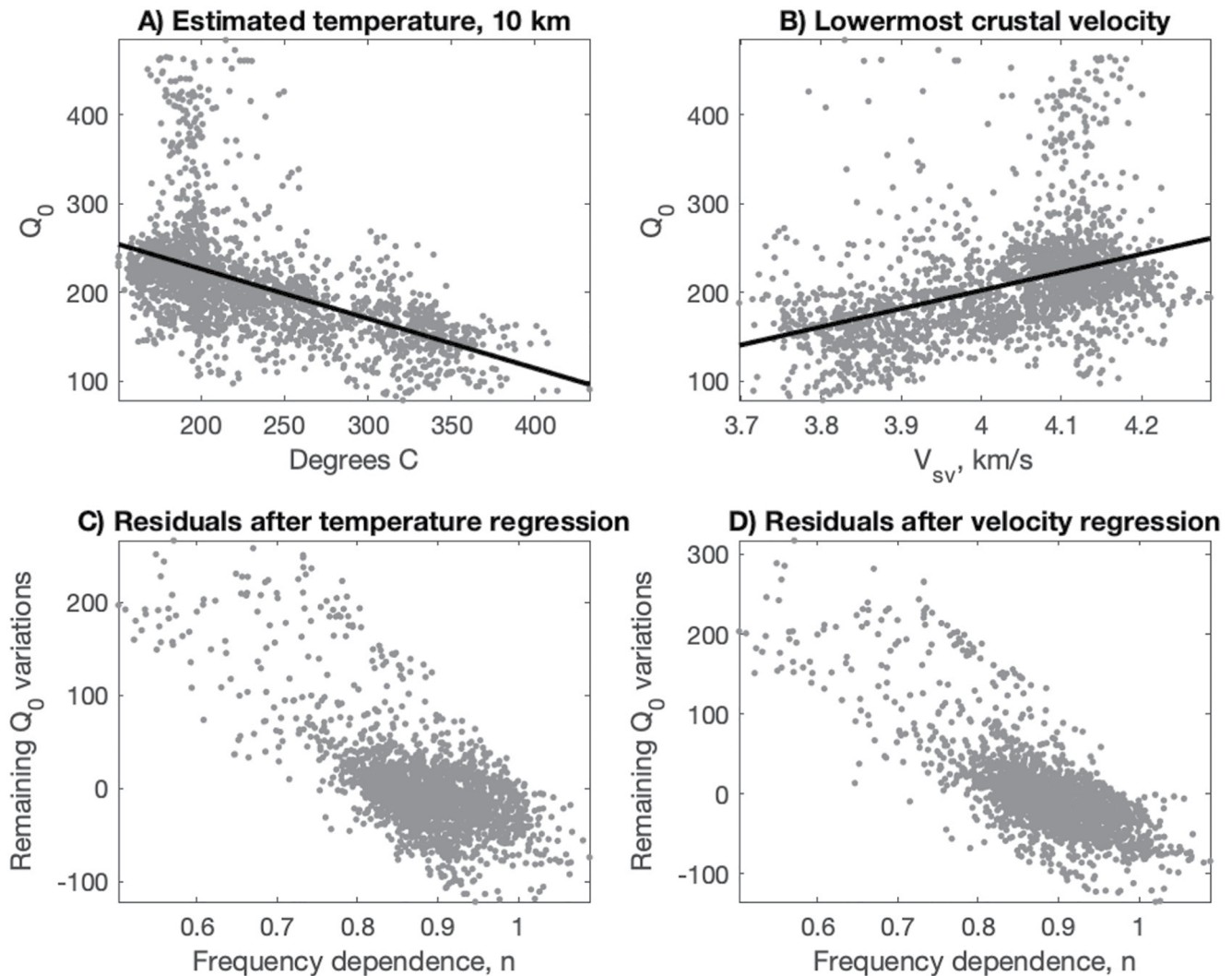


**Figure 7.** Comparison of attenuation with other crustal properties. (a)  $1/Q_0$  versus estimated temperature at 10 km depth from heat flow (Blackwell et al., 2011). Best-fit linear regression is shown. (b)  $1/Q_0$  versus shear velocity averaged over the lower 5 km of the crust (Shen & Ritzwoller, 2016). (c and d) Residuals with respect to regressions in (a) and (b). If temperature and velocity may be proxies for intrinsic attenuation, these residuals are possibly interpreted as scattering. Areas in which  $Q$  is more frequency-dependent empirically have higher attenuation than is predicted from temperature or velocity, implying a larger non-thermal (e.g., scattering) component of attenuation. *Note.* The high correlation between residuals and  $\eta$ , semi-quantitatively suggesting that  $\eta$  may scale with scattering intensity (see also Mayeda et al., 1992).

(Blackwell et al., 2011) and shear velocity averaged over the 5 km above the Moho (from the model of Shen & Ritzwoller, 2016). The correlation coefficient between  $1/Q_0$  and the temperature estimate at 10 km depth is 0.63, and a simple linear regression of attenuation onto 10-km temperature explains 41% of the variance in  $1/Q_0$ . We find a similar but weaker signal—correlation coefficient of 0.47 and variance reduction of 25%—with regressions of  $1/Q_0$  onto lowermost crustal velocity (Figure 7d). We hypothesize that the degree to which  $1/Q$  correlates with crustal temperatures and velocity structure represents the contribution of intrinsic attenuation to the heterogeneity in total attenuation.

A corollary to this hypothesis is that the variations in  $1/Q$  that cannot be explained by thermochemical structure are attributed to the intensity of scattering attenuation. A simple test of this corollary can be performed. The regression of total  $Q$  onto temperature or velocity is purported to capture the contribution of intrinsic attenuation; residual  $Q$  variations (Figures 7c and 7d) are implicitly due to scattering and therefore could correlate positively with  $n$ . Indeed, the relationship between  $n$  and residual  $1/Q_0$  variations is stronger still than the relationships between  $1/Q_{\text{total}}$  and temperature or lowermost crustal velocity. Even though the relative contributions at any given

point are subject to the appreciable uncertainty of  $Q_0$  and projected temperature, for example, this line of reasoning and this quantitative test support our suggestion that the short-wavelength areas of high  $n$  and anomalously low  $Q$  highlight zones of high scattering attenuation, whereas the broad patterns away from these zones result from variations in intrinsic attenuation among crustal blocks.

#### 4.9. Regionalization

The primary aim of this study was to refine our understanding of how and where the well documented change in  $Q$  between the nominally stable CEUS and Cenozoic-active WUS takes place. The USGS NSHM uses different ground motion prediction equations in the CEUS and WUS, influencing seismic hazard assessments for a population of ~20 million and building codes for the rapidly growing region. Because attenuation studies targeting the CEUS/WUS boundary have not previously been completed, the current NSHM attenuation boundary (after Frankel et al., 1996; Figure 3a) was drawn from several geophysical and seismotectonic proxies, chief among them historical seismicity rates. Therefore, it is important and potentially impactful to compare the tomographically delineated boundary with the NSHM estimate. The two generally align, especially along the Colorado Plateau/Basin and Range boundary (i.e., the Wasatch Front) and to the north. Both also carve out the Colorado Plateau interior and Wyoming Craton to be included in the CEUS while placing the Rio Grande Rift with the WUS. The NSHM boundary does include a portion of the southern/central Rocky Mountains (Colorado) in WUS, yet the high attenuation zone associated with the Rockies extends ~250 km farther north than the current boundary, leaving only a narrow (~200 km) bridge of high- $Q$  joining the Colorado Plateau and Wyoming Craton. High attenuation also appears to spill over the present boundary onto the Great Plains and into western Wyoming, though some amount of this spillover may be the result of smoothing in the tomographic inversion. Single-event amplitude versus distance transects similar to those used by Cramer (2018) on the Gulf Coast could delineate attenuation changes more precisely and thus refine the boundary further.

Despite the first-order CEUS/WUS dichotomy, the interior of North America cannot simply be regionalized as East and West, however. The CEUS is indeed comparatively homogeneous (with the major exception of the Gulf Coast), but in areas of major previous tectonism—the Yavapai-Mazatzal suture, the MCR, and the Mississippi Embayment—there appear to be moderately low- $Q$  anomalies. Other features, such as the northern and eastern portions of the MCR, the Grenville Front, and the Appalachians, may host similar  $Q$  anomalies (e.g., Gallegos et al., 2014; Zhao & Mousavi, 2018), but these areas lie beyond the region of our primary interest in the present work.

The complexity of  $Q$  structure suggests that it would be beneficial to consider path-dependent attenuation models when producing ground motion predictions and forecasts. For example, different amplitudes of shaking are expected at a site in the eastern Basin and Range due to a Basin and Range earthquake 200 km to the west and a Colorado Plateau earthquake 200 to the east. Intuition may suggest that the Plateau event would generate higher ground motions because of the high  $Q$  in the Plateau, but between source and site the energy must cross the very low- $Q$  boundary between the two provinces. To illustrate with approximate scenario values, the first 50 km of the path has  $Q_0 \sim 250$ , then it traverses a 100-km zone of  $Q_0 \sim 100$ , and finally 50 km of  $Q_0 \sim 175$  (see Figure 3a). The distance-averaged  $1/Q_0$  for this hypothetical Lg is 0.0077—effectively equivalent to constant  $Q_0$  of 130 along the path. By contrast, a raypath that starts and stays in the Basin and Range experiences roughly constant  $Q_0$  of 175 ( $1/Q_0 = 0.0057$ ) and, therefore, higher overall ground motions. Detailed path-specific ground motion predictions for source faults may be warranted, and we suggest that refined models of  $Q$  in the IMW, especially, could improve forecasts.

#### 5. Conclusion

We have produced a new model of crustal (Lg) attenuation targeting the central half of the continental United States, with the aim of providing the first targeted imaging of the nature and location of the change from low attenuation in the CEUS to high attenuation in the West. To do so, we leverage the human-induced increase in seismicity rates in the central United States over the past decade and the contemporaneous passage of the USArray. Our crustal attenuation model displays the same broad features as previous models, including higher attenuation in the Basin and Range ( $Q_0 \sim 170$ ) than the Great Plains ( $Q_0 \sim 270$ ) and higher attenuation on the Gulf Coast ( $Q_0 \sim 175$ ) than the rest of the central United States. The West cannot be characterized as a single high-attenuation

region, however. Low attenuation similar to the CEUS characterizes the Colorado Plateau ( $Q_0 \sim 250$ ) and Wyoming Craton ( $Q_0 \sim 230$ ). Attenuation is comparatively weakly dependent on frequency in these provinces, and attenuation correlates with thermal structure and crustal velocity. These lines of evidence suggest that the broad patterns of crustal attenuation within these provinces are most readily ascribed to intrinsic (thermally or lithologically controlled) attenuation. The edges of broadly uniform attenuation provinces are typically sharp, rather than gradational, but attenuation boundaries do not always coincide with physiographic boundaries. For example, high attenuation within the southern Rockies ( $Q_0 \sim 100$ ) extends westward some distance into the physiographic Colorado Plateau but ends abruptly at the eastern range front, at the physiographic boundary with the Great Plains.

Improved resolution reveals that broad regions of internally consistent  $Q$  are separated by very high-attenuation bands ( $Q_0 \sim 100$ ), with peaks in attenuation at these boundaries between provinces. Additional high-attenuation anomalies align with several major tectonic features, including the Yavapai-Mazatzal suture ( $Q_0 \sim 160$ ), the MCR ( $Q_0 \sim 200$ ), and the Mississippi Embayment ( $Q_0 \sim 130$ ). Attenuation is more strongly frequency dependent in these boundary/deformation zones. Furthermore, we find that the relationship between thermal structure and attenuation breaks down in these areas, such that attenuation is higher than predicted by a linear  $1/Q_0$ -temperature regression. We interpret these characteristics as indicative of a relatively larger component of scattering attenuation, which sums with intrinsic attenuation and therefore increases both total attenuation and frequency dependence.

The heterogeneity in attenuation structure defies a simple East versus West regionalization. Improvements in ground motion predictions could be realized with finer-scale models that include refined estimates of the locations and magnitudes of changes in attenuation. Additionally, we find that predicted ground motions can be rather strongly path-dependent, implying that the most robust estimates of shaking amplitudes require path-specific attenuation models. Improved regionalized attenuation studies are critical to improving ground shaking predictions and their lateral variation, and models based on the modified attenuation relations are needed to improve seismic hazard estimates across the country.

## Data Availability Statement

No new or proprietary data was used in this study. Waveforms were obtained from IRIS: <https://www.iris.edu>. Tomography codes and amplitude data/metadata are available at <https://github.com/WillLevandowski/LgQTomography>. They are also archived at <https://zenodo.org/record/5570878#.YWizDC1h3OQ> in accordance with AGU requirements. Only the GitHub versions will be maintained. Final  $Q$  models, empirical receiver terms and receiver metadata, empirical source terms and source metadata, and jackknife uncertainties are included as Supporting Information S1.

## Acknowledgments

The authors thank Claire Perry, Morgan Moschetti, Chris Cramer, Brian Shiro, two anonymous reviewers, Associate Editor Martha Savage, and Associate Editor Michael Bostock for their comments on various versions of this manuscript. Funding was provided by USGS EHP Award G18AP00069 to W. Levandowski prior to his joining Tetra Tech, which is not affiliated with this work. D. AbdelHameid was funded by a RESESS internship through UNAVCO.

## References

- Abrams, G. M., & Knepper, D. H., Jr. (1994). *Complete Bouguer gravity anomaly, isostatic-residual gravity, horizontal gradient, and terrain maps of Colorado* (USGS Geophysical Investigations Map 1009). USGS. <https://doi.org/10.3133/gp1009>
- Baer, S., & Mitchell, B. J. (1998). Regional variation of Lg coda  $Q$  in the continental United States and its relation to crustal structure and evolution. *Pure and Applied Geophysics*, 153, 613–638. <https://doi.org/10.1007/s000240050210>
- Benz, H. M., Frankel, A., & Boore, D. M. (1997). Regional Lg attenuation for the continental United States. *Bulletin of the Seismological Society of America*, 87(3), 606–619. <https://doi.org/10.1785/bssa0870030606>
- Berglund, H. T., Sheehan, A. F., Murray, M. H., Roy, M., Lowry, A. R., Nerem, S., & Blume, F. (2012). Distributed deformation across the Rio Grande Rift, Great Plains, and Colorado Plateau. *Geology*, 40, 23–26. <https://doi.org/10.1130/G32418.1>
- Blackwell, D., Richards, M., Frone, Z., Ruzo, A., & Dingwall, R. (2011). Temperature-at-depth maps for the conterminous US and geothermal resource estimates. *Geothermal Resources Council - Transactions*, 35, 1545–1550.
- Bolhnger, G. A. (1979). *Attenuation of the Lg phase and the determination of Mb M the Southeastern United States* (Vol. 69, pp. 45–62). Bulletin of the Seismological Society of America.
- Boyd, O. S., Sheehan, A. F., Karlstrom, K. E., & Keller, G. R. (2005). Attenuation tomography beneath the Rocky Mountain Front: Implications for the physical state of the upper mantle. In K. E. Karlstrom, & G. R. Keller (Eds.), *The Rocky mountain region—An evolving lithosphere: Tectonics, geochemistry, and geophysics* (Vol. 154). AGU Monograph. <https://doi.org/10.1029/154gm27>
- Brandenburg, W. E., Levandowski, W., Califf, T. C., Manly, C., & Levandowski, C. B. (2017). Animal, microbial, and fungal borne skin pathology in the mountain wilderness: A review. *Wilderness and Environmental Medicine*, 29(2), 127–138. <https://doi.org/10.1016/j.wem.2017.02.007>
- Brune, J. N. (1970). Tectonic stress and the spectra of seismic shear waves from earthquakes. *Journal of Geophysical Research*, 75, 4997–5009. <https://doi.org/10.1029/jb075i026p04997>
- Brune, J. N. (1971). Correction. *Journal of Geophysical Research*, 76, 5002.
- Burberry, C. M., Joeckel, R. M., & Korus, J. T. (2015). Post-Mississippian tectonic evolution of the Nemaha Tectonic Zone and Midcontinent Rift System, SE Nebraska and N Kansas. *Mountain Geologist*, 52(4), 47–73.



- Cramer, C. H. (2017). Gulf Coast regional  $Q$  and boundaries from USArray Data. *Bulletin of the Seismological Society of America*, 108(1), 437–449. <https://doi.org/10.1785/0120170170>
- Cramer, C. H. (2018). Gulf Coast Regional  $Q$  and boundaries from USArray data. *Bulletin of the Seismological Society of America*, 108(1), 437–449. <https://doi.org/10.1785/0120170170>
- Crone, A. J., Machette, M. N., Bradley, L.-A., & Mahan, S. A. (1997). *Late quaternary surface faulting on the Cheraw Fault, Southeastern Colorado* (USGS Miscellaneous Investigations Map IMAP 2591). US Geological Survey.
- Davis, D. W., & Green, J. C. (1997). Geochronology of the North American Midcontinent rift in western Lake Superior and implications for its geodynamic evolution. *Canadian Journal of Earth Sciences*, 34(4), 476–488. <https://doi.org/10.1139/e17-039>
- Davis, L. L., & Smith, D. (1993). Ni-rich olivine in minettes from Two Buttes, Colorado: A connection between potassic melts from the mantle and low Ni partition coefficients. *Geochimica et Cosmochimica Acta*, 57, 123–129. [https://doi.org/10.1016/0016-7037\(93\)90473-a](https://doi.org/10.1016/0016-7037(93)90473-a)
- Dwyer, J. J., Herrmann, R. B., & Nuttli, O. W. (1983). Spatial attenuation of the Lg wave in the central United States. *Bulletin of the Seismological Society of America*, 73(3), 781–796. <https://doi.org/10.1785/bssa0730030781>
- Erickson, D., McNamara, D. E., & Benz, H. M. (2004). Frequency-dependent Lg  $Q$  within the continental United States. *Bulletin of the Seismological Society of America*, 94(5), 1630–1643.
- Feucht, D. W., Sheehan, A. F., & Bedrosian, P. A. (2017). Magnetotelluric imaging of lower crustal melt and lithospheric hydration in the Rocky Mountain Front transition zone, Colorado, USA. *Journal of Geophysical Research: Solid Earth*, 122. <https://doi.org/10.1002/2017JB014474>
- Frankel, A., Mueller, C. S., Barnhard, T., Perkins, D., Leyendecker, E. V., Dickman, N., et al. (1996). *National seismic hazard maps—Documentation June 1996*. US Geological Survey.
- Gallegos, A., Ranasinghe, N., Ni, J., & Sandvol, E. (2014). Lg attenuation in the central and eastern United States as revealed by the Earthscope Transportable Array. *Earth and Planetary Sciences Letters*, 402, 187–196. <https://doi.org/10.1016/j.epsl.2014.01.049>
- Gallegos, A., Ranasinghe, N., Ni, J., & Sandvol, E. (2017). Lg attenuation, frequency dependence and relative site response of the western United States as revealed by the Earthscope Transportable Array. *Geophysical Journal International*, 209(3), 1955–1971. <https://doi.org/10.1093/gji/ggx145>
- Gordon, M. B., & Hempton, M. R. (1986). Collision-induced rifting: The Grenville Orogeny and the Keweenaw Rift of North America. *Tectonophysics*, 127(1–2), 1–25. [https://doi.org/10.1016/0040-1951\(86\)90076-4](https://doi.org/10.1016/0040-1951(86)90076-4)
- Hammond, W. C., & Humphreys, E. D. (2000). Upper mantle seismic wave attenuation: Effects of realistic partial melt distribution. *Journal of Geophysical Research: Solid Earth*, 105(B5), 10975–10986.
- Herrmann, R. B. (1980).  $Q$  estimates using the coda of local earthquakes. *Bulletin of the Seismological Society of America*, 70, 447–468.
- Lee, C. T., Yin, Q., Rudnick, R. L., & Jacobsen, S. B. (2001). Preservation of ancient and fertile lithospheric mantle beneath the southwestern United States. *Nature*, 411, 69–73. <https://doi.org/10.1038/35075048>
- Leonard, E. M. (2002). Geomorphic and tectonic forcing of late Cenozoic warping of the Colorado piedmont. *Geology*, 30, 595–598.
- Levandowski, W., Herrmann, R. B., Briggs, R., Boyd, O. S., & Gold, R. (2018). An updated stress map of the continental United States reveals heterogeneous intraplate stress. *Nature Geoscience*, 11, 433–437. <https://doi.org/10.1038/s41561-018-0120-x>
- Levandowski, W., Jones, C. H., Butcher, L. A., & Mahan, K. H. (2018). Lithospheric density models reveal evidence for Cenozoic uplift of the Colorado Plateau and Great Plains by lower-crustal hydration. *Geosphere*, 14(3), 1150–1164. <https://doi.org/10.1130/GES01619.1>
- Levandowski, W., Zellman, M., & Briggs, R. (2017). Gravitational body forces focus North American intraplate earthquakes. *Nature Communications*, 8, 14314. <https://doi.org/10.1038/ncomms14314>
- Madariaga, R. (1976). Dynamics of an expanding circular fault. *Bulletin of the Seismological Society of America*, 66(3), 639–666.
- Mayeda, K., Koyanagi, S., Hoshiba, M., Aki, K., & Zeng, Y. (1992). A comparative study of scattering, intrinsic, and coda  $Q - 1$  for Hawaii, Long Valley, and Central California between 1.5 and 15.0 Hz. *Journal of Geophysical Research*, 97, 6643–6659. <https://doi.org/10.1029/91JB03094>
- McNamara, D. E., Gee, L., Benz, H. M., & Chapman, M. (2014). Frequency-dependent seismic attenuation in the eastern United States as observed from the 2011 central Virginia earthquake and aftershock sequence. *Bulletin of the Seismological Society of America*, 104(1), 55–72. <https://doi.org/10.1785/0120130045>
- McNamara, D. E., Owens, T. J., & Walter, W. R. (1996). Propagation characteristics of Lg across the Tibetan Plateau. *Bulletin of the Seismological Society of America*, 86, 457–469.
- McNamara, D. E., & Walter, W. R. (2001). Mapping crustal heterogeneity using Lg propagation efficiency throughout the Middle East, Mediterranean southern Europe and northern Africa. *Pure and Applied Geophysics*, 158, 1165–1188.
- McWilliams, M. O., & Dunlop, D. J. (1978). Grenville paleomagnetism and tectonics. *Canadian Journal of Earth Sciences*, 15(5), 687–695. <https://doi.org/10.1139/e78-076>
- Miller, J. D., Green, J. C., Severson, M. J., Chandler, V. W., Hauck, S. A., Peterson, D. M., & Wahl, T. E. (2002). *Geology and mineral potential of the Duluth complex and related rocks of Northeastern Minnesota*. MN Geological Survey.
- Mitchell, B., Cong, L., & Jemberie, A. (2015). Continent-wide maps of Lg coda  $Q$  for North America and their relationship to crustal structure and evolution. *Bulletin of the Seismological Society of America*, 105, 409–419.
- Morozov, I. B. (2008). Geometrical attenuation, frequency dependence of  $Q$ , and the absorption band problem. *Geophysical Journal International*, 175, 239–252.
- Mueller, C. S. (2019). Earthquake catalogs for the USGS National Seismic Hazard Maps. *Seismological Research Letters*, 90(1), 251–261. <https://doi.org/10.1785/0220170108/4602968/srl-2017108>
- Nuttli, O. (1973). Seismic wave attenuation and magnitude relations for eastern North America. *Journal of Geophysical Research*, 78(5), 876–885.
- Pasyanos, M. E. (2013). A lithospheric attenuation model of North America. *Bulletin of the Seismological Society of America*, 103, 3321–3333.
- Pasyanos, M. E., Matzel, E. M., Walter, W. R., & Rodgers, A. J. (2009). Broadband Lg attenuation modelling in the Middle East. *Geophysical Journal International*, 177, 1166–1176.
- Petersen, M. D., Moschetti, M. P., Powers, P. M., Mueller, C. S., Haller, K. M., Frankel, A. D., et al. (2014). *Documentation for the 2014 update of the United States National Seismic Hazard Maps*. U.S. Geological Survey.
- Petersen, M. D., Mueller, C. S., Moschetti, M. P., Hoover, S. M., Llenos, A. L., Ellsworth, W. L., et al. (2016). *2016 one-year seismic hazard forecast for the central and eastern United States from induced and natural earthquakes*. U.S. Geological Survey.
- Pyle, M. L., Walter, W. R., & Pasyanos, M. E. (2017). High-resolution Lg and Pg attenuation models in the Basin and Range, with implications for frequency-dependent  $Q$ . *Bulletin of the Seismological Society of America*, 107(6), 2846–2858. <https://doi.org/10.1785/0120170172>
- Roy, M., Jordan, T. H., & Pedersen, J. (2009). Colorado Plateau magmatism and uplift by warming of heterogeneous lithosphere. *Nature*, 459. <https://doi.org/10.1038/nature08052>
- Sato, T., & Hirasawa, T. (1973). Body wave spectra from propagating shear cracks. *Journal of Physics of the Earth*, 21, 415–431.
- Savage, J. C. (1972). Relation of corner frequency to fault dimensions. *Journal of Geophysical Research*, 77, 3788–3795.

- Shen, W., & Ritzwoller, M. H. (2016). Crustal and upper mantle structure beneath the United States. *Journal of Geophysical Research*, 121, 4306–4342. <https://doi.org/10.1002/2016JB012887>
- Singh, S. (1981). *Regionalization of crustal Q in the continental United States (Ph.D. dissertation)*. Saint Louis University.
- Singh, S., & Herrmann, R. B. (1983). Regionalization of crustal coda *Q* in the continental United States. *Journal of Geophysical Research*, 88(B1), 527–538.
- Stein, C. A., Stein, S., Merino, M., Keller, G. R., Flesch, L. M., & Jurdy, D. M. (2014). Was the Midcontinent Rift part of a successful sea-floor-spreading episode? *Geophysical Research Letters*, 415, 1465–1470.
- USGS. (2016). *Moment tensors*. USGS. Retrieved from <https://earthquake.usgs.gov/earthquakes/search/>
- Vervoort, J. D., Wirth, K., Kennedy, B., Sandland, T., & Harpp, K. S. (2007). The magmatic evolution of the Midcontinent rift: New geochronologic and geochemical evidence from felsic magmatism. *Precambrian Research*, 157(1–4), 235–268. <https://doi.org/10.1016/j.precamres.2007.02.019>
- Walter, W. R., & Taylor, S. R. (2001). *A revised magnitude and distance amplitude correction (MDAC2) procedure for regional seismic discriminants: Theory and testing at NTS*. Lawrence Livermore National Laboratory. Retrieved from <http://www.llnl.gov/tid/lof/documents/pdf/240563.pdf>
- Whitmeyer, & Karlstrom (2007). Tectonic model for the Proterozoic growth of North America. *Geosphere*, 3(4), 220–259. <https://doi.org/10.1130/GES00055.1>
- Zellman, M. S., Ostenaar, D. A., & Brown, M. (2021). Subsurface characterization of the quaternary active Cheraw Fault in southeastern Colorado based on seismic imaging. *The Seismic Record*, 1(1), 56–65. <https://doi.org/10.1785/0320210016>
- Zhao, L.-F., & Mousavi, S. M. (2018). Lateral variations of crustal *L<sub>g</sub>* attenuation across eastern North America. *Scientific Reports*, 8, 7285. <https://doi.org/10.1038/s41598-018-25649-5>

## References From the Supporting Information

- Darragh, R., Wong, I., & Silva, W. (2019). Evaluating kappa, *Q*(*f*), and stress parameter in the Rocky Mountains of Central Colorado. *Bulletin of the Seismological Society of America*, 109(2), 586–599. <https://doi.org/10.1785/0120180122>
- Efron, B., & Tibshirani, R. J. (1993). *An introduction to the bootstrap*. CRC Press.